INTERNATIONAL JOURNAL FOR NUMERICAL METHODS IN FLUIDS
Int. J. Numer. Meth. Fluids 2008; **56**:525–555
Published online 24 July 2007 in Wiley InterScience (www.interscience.wiley.com). DOI: 10.1002/fld.1540

Reynolds-stress modelling of $M = 2.25$ shock-wave/turbulent boundary-layer interaction

I. Vallet*, †

Institut d'Alembert, Université Pierre et Marie Curie-Paris 6, case 161, 4 place Jussieu, 75005 Paris, France

SUMMARY

$M = 2.25$ shock-wave/turbulent-boundary-layer interactions over a compression ramp for several angles (8, 13 and 18°) at Reynolds-number $Re_{\theta_0} = 7 \times 10^3$ were simulated with three low-Reynolds second-moment closures and a linear low-Reynolds standard k–ε model. A detailed assessment of the turbulence closures by comparison with both mean-flow and turbulent experimental quantities is presented. The Reynolds-stress model which is wall-topology free and which uses an optimized redistribution closure, is in good agreement with experimental data both for wall-pressure and mean-velocity profiles. Detailed analysis of three components of the Reynolds-stress tensor (comparison with measurements and transport-equation budgets) provides a critical evaluation of full Reynolds-stress models for the separated supersonic compression ramp. The discrepancy observed in the shock-wave foot region, between computations and measurements for the Reynolds-stresses profiles, could be explained by considering the experimental shock-wave oscillation and directions for future modelling work are indicated. Copyright © 2007 John Wiley & Sons, Ltd.

Received 16 November 2006; Revised 16 April 2007; Accepted 6 May 2007

KEY WORDS: Reynolds-stress model; shock-wave; supersonic flows; separation zone

1. INTRODUCTION

Numerous previous works [1–15] have highlighted the difficulty to predict numerically shock-wave/turbulent-boundary-layer interactions in supersonic compression corner flows.

Low-Reynolds number standard eddy-viscosity models are not adapted to predict supersonic flows with a large separation zone. Knight *et al.* [12], Haidinger and Friedrich [4], Dolling [7], Gerolymos *et al.* [13], Liou *et al.* [8] and Sinha *et al.* [15] have shown that linear two-equation closures, such as the k–ε models of Chien [16], Jones and Launder [17], and Launder and Sharma [18] or the k–ω model of Wilcox [19], underestimate the upstream influence for the

*Correspondence to: I. Vallet, Institut d'Alembert, Université Pierre et Marie Curie, case 161, 4 place Jussieu, 75005 Paris, France.
†E-mail: vallet@ccr.jussieu.fr

24° compression ramp of Settles *et al.* [20]. Rizzetta [6] reached the same conclusion with the k–ε model of Jones and Launder [21] for the 24-deg compression ramp of Kuntz *et al.* [22]. In accordance with the unsatisfactory wall-pressure prediction, all of the linear two-equation models assessed underpredict the mean-flow velocity profiles, especially upstream of the corner. On the contrary, the k–ζ model developed by Robinson and Hassan [23] predicts the correct wall-pressure distribution for the 25-deg compression ramp of Zheltovodov *et al.* [24], but severely overpredicts the axial mean-flow velocity in the recovery region [11]. The q–ω model of Coakley and Huang [25], assessed by Gerlinger and Brüggemann [26], gives the same kind of results for the 24-deg compression ramp of Settles *et al.* [20]. Liou *et al.* [8] assessed the zonal k–ε/k–ω model of Menter [27] for the compression ramps of Settles *et al.* [20]. The model of Menter [27] is in good agreement with experimental data for the 8- and 16-deg compression-ramp angles which do not present detached flows, but overestimates the separation zone for the 20- and 24-deg angles.

Explicit algebraic Reynolds-stress models (EARSM), such as the model of Craft *et al.* [28] and the model of Gatski and Speziale [29] and Abid *et al.* [30], generally overpredict the recirculation zone. This overprediction becomes more pronounced with increasing compression-ramp angle [6, 9]. Rizzetta [6] considers that the EARSM offers little improvement over 0-, 1- and 2-equation closures. Matesanz and Velazquez [9] proposed an EARSM based on the model of Abid *et al.* [30] with the compressibility correction of Wilcox [31], which predicts quite well the recirculation zone for the 20-deg compression ramp of Settles *et al.* [20]. Nevertheless, Matesanz and Velazquez [9] concluded that full Reynolds-stress model (RSM) are more accurate than algebraic Reynolds-stress models.

Indeed, it seems that only more elaborate statistical turbulence models have the ability to predict the large separation zone experimentally observed at important compression-ramp angles. The multiscale k–ω model of Wilcox [1], the RSM of Haidinger and Friedrich [4], which uses the ω-equation of Wilcox [32], and the RSM of Gerolymos and Vallet [33], give similar results for the 20-deg and the 24-deg compression ramps of Settles *et al.* [20]. Note that both these second-moment closures are fully wall-topology free (these models do not use any wall-function, normal to the wall or distance from the wall), and the RSM developed by Haidinger and Friedrich [4] contains compressibility effects. These three advanced turbulence closures are in good agreement with experimental data for the wall-pressure distribution and slightly overpredict the mean-flow velocity near the wall ($y/\delta_0 < 0.4$) downstream the shock-wave interaction [1, 5, 7, 34]. Concerning the Reynolds stresses distributions, few comparisons between computation and experiments have been published [4, 6] mainly because of the lack of measurements. The predictions of Reynolds-stresses profiles obtained using EARSM [6] or RSM [4] are generally not in very good agreement with experimental data.

To overcome these discrepancies, Rizzetta and Visbal [10] chose to make a great progress by using large-eddy simulation (LES). Indeed, the unsteadiness of the shock wave in supersonic compression corner flows has been observed experimentally by several authors whose studies are described in detail by Dolling [7, 35] and Knight *et al.* [12]. Unfortunately, certainly because of the substantially lower than experimental Reynolds number, the LES predictions were not better than advanced RANS models [1, 5, 7, 34] for the four compression-ramp angles of Settles *et al.* [20]. On the contrary the upstream influence was slightly overestimated except for the 24-deg angle case, and the Reynolds stresses profiles were not in good agreement with experimental data.

More recently, an hybrid LES/k–ζ model was developed by Xiao *et al.* [11] and assessed for the compression ramp of Zheltovodov *et al.* [24]. This model improves the prediction of the

DOI: 10.1002/fld

mean-flow velocity profiles in the recovery region, but the RANS model of Robinson and Hassan [23] is in better agreement with experimental data in the separated flow region. Finally, Sinha *et al.* [15] proposed a shock-unsteadiness modification to the linear two-equation RANS models of Wilcox [19] and of Launder and Sharma [18]. The modified models are in better agreement with experimental data of Settles *et al.* [20], but fail to predict the correct upstream influence for any of the compression-ramp angles (16, 20 and 24°). However, it should be kept in mind, that most of the experimental data used [20, 22, 24] are time averaged, and as Dolling [7, 35] recommended, it is important to understand both the turbulence-model limitations and how the experimental data were generated, before providing any conclusion. Furthermore, none of the turbulence-model reviews [7, 8, 12] have considered the predictions obtained by using full Reynolds-stress models.

The purpose of the present paper is to analyse comparisons between measurements and computations using various low-Reynolds number near-wall Reynolds-stress and k–ε models, for several compression-ramp angles with particular emphasis on the turbulence structure prediction. The compression-ramp configurations examined were studied experimentally by Ardonceau [36]. This experimental database is interesting because both mean-flow and Reynolds-stresses experimental distributions are available for three compression-ramp angles. Furthermore, the channel is large enough to consider that the experimental data are reasonably free of 3-D effects. The near-wall wall-topology-free RSM developed by Gerolymos and Vallet [33] was compared to the Launder and Shima [37] RSM (which uses geometric wall normals and distances from the wall) and its wall-topology-free version [34] for each configuration. The linear Launder and Sharma k–ε closure [18] was used for comparison because its predictions are typical of two-equation closures. The redistribution-term impact (missing in two-equation closures) is evaluated through detailed comparisons with experimental data of the Reynolds stresses profiles and transport-equation budgets analysis. All computations were carefully checked for grid convergence for all of the turbulence closures used, and with identical experimental inflow conditions. The performance of the various models used (which are described in detail to enhance understanding of the computational results), is carefully assessed and the link with the experimental unsteadiness induced shock-wave oscillation and its consequences is mentioned.

2. TURBULENCE CLOSURES

2.1. Mean-flow model

The flow is modelled by the compressible Favre–Reynolds-averaged 3-D Navier–Stokes equations. Denoting t the time, x_ℓ the Cartesian space coordinates, u_i the velocity components, ρ the density, p the pressure, δ_{ij} the Kronecker symbol, τ_{ij} the viscous stresses, $\widetilde{(\cdot)}$ Favre-averaging, $\overline{(\cdot)}$ non-weighted-averaging (or Reynolds-averaging), $(\cdot)''$ Favre-fluctuations and $(\cdot)'$ non-weighted-fluctuations (for any flow quantity $b=\tilde{b}+b''=\bar{b}+b'$ and for any flow quantities [38] b_1 and b_2: $\overline{b_1''b_2'}\equiv\overline{b_1'b_2'}\equiv\overline{b_1'b_2''}$). The symbol $\breve{(\cdot)}$ is used to denote a function of average quantities that is neither a Favre-average nor a non-weighted average

$$\frac{\partial\bar{\rho}}{\partial t}+\frac{\partial\bar{\rho}\tilde{u}_\ell}{\partial x_\ell}=0 \tag{1}$$

DOI: 10.1002/fld

$$\frac{\partial \bar{\rho}\tilde{u}_i}{\partial t} + \frac{\partial(\bar{\rho}\tilde{u}_i\tilde{u}_\ell)}{\partial x_\ell} = -\frac{\partial \bar{p}}{\partial x_i} + \frac{\partial}{\partial x_\ell}[\bar{\tau}_{i\ell} - \widetilde{\bar{\rho}u_i''u_\ell''}] \tag{2}$$

$$\frac{\partial(\bar{\rho}\breve{h}_t - \bar{p})}{\partial t} + \frac{\partial(\bar{\rho}\tilde{u}_\ell\breve{h}_t)}{\partial x_\ell} = \frac{\partial}{\partial x_\ell}[\tilde{u}_i(\bar{\tau}_{i\ell} - \widetilde{\bar{\rho}u_i''u_\ell''}) - (\bar{q}_\ell + \widetilde{\bar{\rho}h''u_\ell''})] - S_{\breve{h}_t} \tag{3}$$

with

$$S_{\breve{h}_t} = \underbrace{\widetilde{\bar{\rho}u_i''u_\ell''}\frac{\partial \tilde{u}_i}{\partial x_\ell}}_{-P_k = -\frac{1}{2}P_{mm}} + \underbrace{\overline{\tau'_{i\ell}\frac{\partial u_j''}{\partial x_\ell}}}_{\bar{\rho}\varepsilon = \frac{1}{2}\bar{\rho}\varepsilon_{mm}} + \frac{\partial[\overline{p'u'_\ell}]}{\partial x_\ell} - \overline{p'\frac{\partial u'_\ell}{\partial x_\ell}} + \overline{u_\ell''}\frac{\partial \bar{p}}{\partial x_\ell} + \overline{\tau_{i\ell}}\frac{\partial \overline{u_i''}}{\partial x_\ell} \tag{4}$$

We preferred to solve a transport equation for the total enthalpy of the mean flow $\breve{h}_t = \tilde{h} + \frac{1}{2}\tilde{u}_i\tilde{u}_i$ rather than for the Favre-averaged total enthalpy $\tilde{h}_t = \breve{h}_t + k$ (h is the specific enthalpy, and $k = \frac{1}{2}\widetilde{u_i'''u_i''}$ is the turbulent kinetic energy). Indeed, this involves a link between the source term in the mean energy equation $S_{\breve{h}_t}$ and the turbulent kinetic energy transport equation (which is the trace of the Reynolds-stress transport equations), and simplifies the closure of the mean energy transport equation. Neglecting the density-fluctuation effect $\overline{u_i''}$ ($\overline{u_i''} \equiv \bar{u}_i - \tilde{u}_i = -\overline{\rho' u_i''}/\bar{\rho}$ represents direct compressibility effects), the pressure diffusion term $\partial\overline{p'u'_\ell}/\partial x_\ell$ and the pressure-dilatation correlation $\overline{p'(\partial u'_\ell/\partial x_\ell)}$, the source term in the mean energy equation is simplified by

$$S_{\breve{h}_t} \cong -(P_k - \bar{\rho}\varepsilon) \tag{5}$$

where P_k and ε are, respectively, the production and the dissipation rate of the turbulent kinetic energy transport equation (Equation (13)).

Neglecting the influence of temperature fluctuations, the mean viscous stress tensor and the molecular heat-flux vector are approximated in the usual way by [38, 39]

$$\bar{\tau}_{i\ell} \cong \breve{\mu}\left(\frac{\partial \tilde{u}_i}{\partial x_\ell} + \frac{\partial \tilde{u}_\ell}{\partial x_i} - \frac{2}{3}\frac{\partial \tilde{u}_m}{\partial x_m}\delta_{i\ell}\right), \quad \breve{\mu} = \mu(\tilde{T}) = \mu_{273}\frac{\tilde{T}^{3/2}}{273.15^{3/2}}\frac{T_S + 273.15}{T_S + \tilde{T}} \tag{6}$$

$$\bar{q}_\ell \cong -\breve{\kappa}\frac{\partial \tilde{T}}{\partial x_\ell}, \quad \breve{\kappa} = \kappa(\tilde{T}) = \kappa_{273}\frac{\mu(\tilde{T})}{\mu_{273}}[1 + A_\kappa(\tilde{T} - 273.15)] \tag{7}$$

All computations were performed for air ($R_g = 287.04\,\mathrm{m^2\,s^{-2}\,K^{-1}}$) considered thermodynamically and calorically perfect ($\bar{p} = \bar{\rho}R_g\tilde{T}$, $\gamma = 1.4$), and we used a Sutherland law dependence for molecular dynamic viscosity $\breve{\mu}$ and a corrected Sutherland law [40] heat conductivity $\breve{\kappa}$ ($\mu_{273} = 17.11 \times 10^{-6}\,\mathrm{Pa\,s}$, $\kappa_{273} = 0.0242\,\mathrm{W\,m^{-1}\,K^{-1}}$, $T_S = 110.4\,\mathrm{K}$, and $A_\kappa = 0.00023\,\mathrm{K^{-1}}$). Thus, the compressibility effect for all of the models studied in the present work, is taken into account by the variation of the mean-flow density $\bar{\rho}$.

By analogy with the molecular heat-flux model, the turbulent heat-flux is closed by a simple gradient model and we used a constant turbulent Prandtl number $Pr_T = 0.9$ to obtain the correct recovery temperature for turbulent flow over an adiabatic wall [38]

$$\widetilde{\bar{\rho}h''u_i''} \cong -\kappa_T\frac{\partial \tilde{T}}{\partial x_i}, \quad \mu_T = 0.09\mathrm{e}^{-3.4/(1+0.02\,Re_T^{*})^2}\breve{\mu}\,Re_T^{*}, \quad Re_T^{*} = \frac{\bar{\rho}k^2}{\breve{\mu}\varepsilon^{*}} \tag{8}$$

DOI: 10.1002/fld

where $c_p = R_g\gamma/(\gamma-1)$ is the heat capacity at constant pressure and Re^*_{T} the turbulent Reynolds number based on the modified dissipation-rate $\varepsilon^* = \varepsilon - 2\check{\nu}(\mathrm{grad}\sqrt{k})^2$ [17]. This closure introduces an eddy-diffusivity $\alpha_{\mathrm{T}} = \nu_{\mathrm{T}}/Pr_{\mathrm{T}}$ and a turbulent Prandtl number $Pr_{\mathrm{T}} = \mu_{\mathrm{T}}c_p/\kappa_{\mathrm{T}}$, which are non-physical quantities as the Boussinesq hypothesis does with the turbulent-viscosity μ_{T} for the Reynolds-stress tensor closure (Equation (14)). An alternative, independent of constant-turbulent-Prandtl-number assumption, is to solve directly transport equations for the turbulent heat fluxes and the temperature variance dissipation rate [5, 41].

2.2. Turbulent transport equations

The exact transport equations for the Favre–Reynolds-averaged Reynolds-stresses are

$$\underbrace{\frac{\partial\bar{\rho}\widetilde{u_i''u_j''}}{\partial t}+\frac{\partial(\bar{\rho}\widetilde{u_i''u_j''}\tilde{u}_\ell)}{\partial x_\ell}}_{\text{convection } C_{ij}}$$

$$=\underbrace{\frac{\partial}{\partial x_\ell}(-\bar{\rho}\widetilde{u_i''u_j''u_\ell''}-\overline{p'u_j''}\delta_{i\ell}-\overline{p'u_i''}\delta_{j\ell}+\overline{u_i''\tau'_{j\ell}}+\overline{u_j''\tau'_{i\ell}})}_{\text{diffusion } d_{ij}}$$

$$+\underbrace{\left(-\bar{\rho}\widetilde{u_i''u_\ell''}\frac{\partial\tilde{u}_j}{\partial x_\ell}-\bar{\rho}\widetilde{u_j''u_\ell''}\frac{\partial\tilde{u}_i}{\partial x_\ell}\right)}_{\text{production } P_{ij}}+\underbrace{\overline{p'\left(\frac{\partial u_i''}{\partial x_j}+\frac{\partial u_j''}{\partial x_i}-\frac{2}{3}\frac{\partial u_k''}{\partial x_k}\delta_{ij}\right)}}_{\text{redistribution } \phi_{ij}}+\underbrace{\frac{2}{3}\overline{p'\frac{\partial u_k''}{\partial x_k}}\delta_{ij}}_{\text{pressure-dilatation } \phi_p}$$

$$-\underbrace{\left(\overline{\tau'_{j\ell}\frac{\partial u_i''}{\partial x_\ell}}+\overline{\tau'_{i\ell}\frac{\partial u_j''}{\partial x_\ell}}\right)}_{\text{dissipation } \bar{\rho}\varepsilon_{ij}}+\underbrace{\left(-\overline{u_i''}\frac{\partial\bar{p}}{\partial x_j}-\overline{u_j''}\frac{\partial\bar{p}}{\partial x_i}+\overline{u_i''}\frac{\partial\bar{\tau}_{j\ell}}{\partial x_\ell}+\overline{u_j''}\frac{\partial\bar{\tau}_{i\ell}}{\partial x_\ell}\right)}_{\text{density fluctuation effects } K_{ij}} \tag{9}$$

Convection, C_{ij}, and production due to the interaction with the mean-flow gradients, P_{ij}, are exact terms, whereas the diffusion $d_{ij} = d^{\mathrm{T}}_{ij} + d^{\mu}_{ij}$ due to turbulent transport $d^{\mathrm{T}}_{ij} = d^{u}_{ij} + d^{p}_{ij}$ and molecular viscosity d^{μ}_{ij}, the pressure-strain redistribution ϕ_{ij} and the dissipation $\bar{\rho}\varepsilon_{ij}$ terms require modelling. In all of the models used, direct compressibility effects K_{ij}, the pressure-diffusion term $d^{p}_{ij} = -\partial(\overline{p'u_j''}\delta_{i\ell} + \overline{p'u_i''}\delta_{j\ell})/\partial x_\ell$, and pressure-dilatation ϕ_p were neglected

$$K_{ij} \cong 0, \quad d^{p}_{ij} \cong 0, \quad \phi_p \cong 0 \tag{10}$$

It is generally accepted [42] that K_{ij} and ϕ_p do not have a major influence in wall-bounded flows and recent work by Pantano and Sarkar [43] indicates that the well-known free-shear-flow major compressibility effect might be due to compressibility damping of ϕ_{ij}. On the contrary, the pressure-diffusion term seems to have substantial influence in 3-D detached and secondary flows [44, 45], but not in 2-D flows except for the friction-skin coefficient downstream of the

DOI: 10.1002/fld

shock-wave/turbulent boundary-layer interaction [44]. If the pressure diffusion term is neglected, the diffusion is approximated by

$$d_{ij} \cong \frac{\partial}{\partial x_\ell}\left[-\bar{\rho}\widetilde{u_i'' u_j'' u_\ell''} + \breve{\mu}\frac{\partial \widetilde{u_i'' u_j''}}{\partial x_\ell}\right] \tag{11}$$

The influence of the pressure-diffusion term is examined in detail in Sauret and Vallet [44] and Vallet [45]. The triple-velocity correlation $-\bar{\rho}\widetilde{u_i'' u_j'' u_\ell''}$, the pressure-strain redistribution ϕ_{ij} and the dissipation $\bar{\rho}\varepsilon_{ij}$ terms modelling are described in Sections 2.4–2.6.

For all of the models studied in the present work, the turbulence-length-scale was determined by solving the Launder and Sharma [18] modified dissipation-rate ε^* equation with the exception of the diffusion term where a tensorial diffusion coefficient is used [46, 47]

$$\frac{\partial \bar{\rho}\varepsilon^*}{\partial t} + \frac{\partial(\tilde{u}_\ell \bar{\rho}\varepsilon^*)}{\partial x_\ell} = \underbrace{\frac{\partial}{\partial x_\ell}\left[C_\varepsilon \frac{k}{\varepsilon^*}\bar{\rho}\widetilde{u_m'' u_\ell''}\frac{\partial \varepsilon^*}{\partial x_m} + \breve{\mu}\frac{\partial \varepsilon^*}{\partial x_\ell}\right]}_{d_\varepsilon = d_\varepsilon^{\mathrm{T}} + d_\varepsilon^{\mu}} + C_{\varepsilon 1} P_k \frac{\varepsilon^*}{k} - C_{\varepsilon 2}\bar{\rho}\frac{\varepsilon^{*2}}{k} + \frac{2\breve{\mu}\mu_{\mathrm{T}}}{\bar{\rho}}(\nabla^2\ \tilde{\mathbf{V}})^2 \tag{12}$$

$$C_\varepsilon = 0.18, \quad C_{\varepsilon 1} = 1.44, \quad C_{\varepsilon 2} = 1.92(1 - 0.3\mathrm{e}^{-Re_{\mathrm{T}}^{*2}})$$

Recent work [48] improves the closure of the dissipation-rate ε-equation ($\varepsilon^* = \varepsilon - 2\breve{\nu}(\mathrm{grad}\sqrt{k})^2$, where $\breve{\nu}$ is the kinematic viscosity, ε is the dissipation rate of the turbulence-kinetic-energy k), especially close to the wall, but from a numerical-stability point of view, it is quite complicated to modify this equation. Indeed, the Dirichlet boundary condition for the modified dissipation rate $\varepsilon^* = 0$ at a solid wall (instead of $\varepsilon = 2\breve{\nu}(\partial\sqrt{k}/\partial n)^2$, where n is the distance from the wall) is compatible with the realizability constraints implementation in the numerical method used [49, 50]. Furthermore, the Jakirlić and Hanjalić modification of the dissipation-rate ε-equation [48] requires a new closure for the dissipation-tensor ε_{ij} in the Reynolds-stress equations. However, in the family of RSMs considered in the present work, the anisotropy of ε_{ij} is modelled together with the slow part of the pressure-strain correlation ϕ_{ij1} (Equations (17) and (26)), and further work is needed to model these two terms separately.

2.3. The Launder and Sharma k–ε model (LS k–ε)

The low-Reynolds-number k–ε closure of Launder and Sharma [18] is used as a baseline eddy-viscosity model prediction. The substantial well-known disadvantages of the k–ε model are mainly due to (1) the use of the Boussinesq hypothesis (Equation (14)), which is based on the analogy with the mean viscous stress tensor law (Equation (6)), and (2) the impossibility to take into account the turbulence anisotropy ($\phi_{mm} = 0$).

This two-equation closure, widely used especially for industrial configurations, solves a transport equation for the turbulent-kinetic energy k

$$\frac{\partial \bar{\rho}k}{\partial t} + \frac{\partial \bar{\rho}k\tilde{u}_\ell}{\partial x_\ell} = \frac{\partial}{\partial x_\ell}\left[\left(\breve{\mu} + \frac{\mu_{\mathrm{T}}}{\sigma_k}\right)\frac{\partial k}{\partial x_\ell}\right] + P_k - \bar{\rho}\varepsilon, \quad \sigma_k = 1 \tag{13}$$

DOI: 10.1002/fld

with the Boussinesq hypothesis for the Reynolds-stress tensor closure present in the mean-flow equation (Equations (2) and (3)) and the production P_k (Equations (4) and (13))

$$-\bar{\rho}\widetilde{u_i'' u_\ell''} \cong \mu_{\mathrm{T}} \left(\frac{\partial \tilde{u}_i}{\partial x_\ell} + \frac{\partial \tilde{u}_\ell}{\partial x_i} - \frac{2}{3} \frac{\partial \tilde{u}_m}{\partial x_m} \delta_{i\ell} \right) - \frac{2}{3} \bar{\rho} k \delta_{i\ell} \tag{14}$$

and a transport equation for the modified dissipation-rate ε^* (Equation (12)) where the turbulent diffusion $d_\varepsilon^{\mathrm{T}}$ is computed as

$$d_\varepsilon^{\mathrm{T}} = \frac{\partial}{\partial x_\ell} \left(\frac{\mu_{\mathrm{T}}}{\sigma_\varepsilon} \frac{\partial \varepsilon^*}{\partial x_\ell} \right), \quad \sigma_\varepsilon = 1.3 \tag{15}$$

2.4. The Launder–Shima–Sharma RSM (LSS RSM)

The Launder–Shima–Sharma Reynolds-stress closure (hereafter LSS RSM) uses the Reynolds-stress closure proposed by Launder and Shima [37] but with the Launder and Sharma [18] modified dissipation-rate ε^*-equation of the k–ε model (Equations (12) and (15)). Indeed, the corrections proposed in the original dissipation-rate ε-equation of Launder and Shima [37] were unsuitable for supersonic or detached flows [51, 52]. The pressure-strain redistribution term is classically [53] split into a slow and a rapid part, and the corresponding echo terms

$$\phi_{ij} = \phi_{ij1} + \phi_{ij2} + \phi_{ij1}^w + \phi_{ij2}^w \tag{16}$$

The slow part ϕ_{ij1} and the dissipation term $\bar{\rho}\varepsilon_{ij}$ were modelled together by using the quasi-linear form proposed by Rotta [54] with a coefficient $C_1 = C_1(Re_{\mathrm{T}}, A_2, A_3)$ suggested by Lumley [55]

$$\begin{aligned} \phi_{ij1} - \bar{\rho}\varepsilon_{ij} &= [\phi_{ij1} - \bar{\rho}\varepsilon_{ij} + \tfrac{2}{3}\bar{\rho}\varepsilon\delta_{ij}] - \tfrac{2}{3}\bar{\rho}\varepsilon\delta_{ij} \\ &= -C_1(Re_{\mathrm{T}}, A_2, A_3)\bar{\rho}\varepsilon a_{ij} - \tfrac{2}{3}\bar{\rho}\varepsilon\delta_{ij} \end{aligned} \tag{17}$$

$$a_{ij} = \frac{\widetilde{u_i'' u_j''}}{k} - \frac{2}{3}\delta_{ij}, \quad A_1 = a_{ii} = 0, \quad A_2 = a_{ik}a_{ki}, \quad A_3 = a_{ik}a_{kj}a_{ji} \tag{18}$$

Thus, the anisotropic part of the dissipation tensor is taken into account through the coefficient C_1, which is a function of the turbulent Reynolds-number Re_{T} and the anisotropy tensor invariants A_2 and A_3 (Equation (18)). Several authors [48, 56–58] have shown, using DNS data [59], that these two terms (ϕ_{ij1} and ε_{ij}) require separate closures especially close to the wall. However, this simplified form (Equation (17)) is numerically very stable at the wall. This increased numerical stability is very practical when computing complex flows over complex geometries [50, 60].

The rapid part closure was proposed by Naot *et al.* [61, 62] which also corresponds to one of the proposals of Launder *et al.* [63]

$$\phi_{ij2} = -C_2(P_{ij} - \tfrac{1}{3}\delta_{ij}P_{mm}) \tag{19}$$

The LSS closure uses the geometric-distance-from-the-wall and the geometric-normal-to-the-wall direction in the echo terms by adopting the closures proposed by Shir [64] for the slow part ϕ_{ij1}^w and by Gibson and Launder [65] for the rapid-part ϕ_{ij2}^w, where f is a damping function calibrated for a flat plate boundary layer by Shir [64] using the von Karman constant κ_{VK}, the turbulent

DOI: 10.1002/fld

length-scale ℓ_T and the distance from the wall n.

$$\phi^w_{ij1} + \phi^w_{ij2} = C^w_1 \frac{\varepsilon}{k}\left[\widetilde{\bar\rho u''_q u''_m} n_q n_m \delta_{ij} - \frac{3}{2}\widetilde{\bar\rho u''_q u''_i} n_q n_j - \frac{3}{2}\widetilde{\bar\rho u''_q u''_j} n_q n_i\right] f + C^w_2\left[\phi_{qm2} n_q n_m \delta_{ij} - \frac{3}{2}\phi_{iq2} n_q n_j - \frac{3}{2}\phi_{jq2} n_q n_i\right] f \tag{20}$$

$$f = \kappa_{VK}\frac{\ell_T}{n}, \quad \kappa_{VK} = 0.4, \quad \ell_T = k^{3/2}\varepsilon^{-1} \tag{21}$$

The improved coefficients proposed by Launder and Shima [37] are functions of the turbulent Reynolds-number Re_T, the second anisotropy tensor invariant A_2, and the flatness parameter $A = 1 - \frac{9}{8}(A_2 - A_3)$ introduced by Lumley [66]

$$C_1 = 1 + 2.58 A A_2^{1/4}[1 - \mathrm{e}^{-(Re_T/150)^2}], \quad C_2 = 0.75\sqrt{A} \tag{22}$$

$$C^w_1 = 1 - \tfrac{2}{3}(C_1 - 1), \quad C^w_2 = \max\left[\frac{2}{3} - \frac{1}{6C_2}, 0\right] \tag{23}$$

The triple-velocity correlation is modelled by the Daly and Harlow [67] proposal

$$-\bar\rho\widetilde{u''_i u''_j u''_\ell} = C_s \frac{k}{\varepsilon}\left(\widetilde{\bar\rho u''_\ell u''_m}\frac{\partial\widetilde{u''_i u''_j}}{\partial x_m}\right), \quad C_s = 0.22 \tag{24}$$

2.5. The Gerolymos and Vallet wall-normal-free RSM (GV RSM)

In complex flows, such as a large recirculation zone, even on a flat plate where the normal to the wall and the distance from the wall can be easily determined, the inhomogeneous part of the flow is not confined to the immediate vicinity of the solid wall. Consequently, the use of conventional echo terms (Equation (20)), with damping functions where geometric parameters appear explicitly, is inappropriate. To account for these effects, it is preferable to split the redistributive term into an homogeneous and an inhomogeneous part following the idea proposed by Craft and Launder [68].

Gerolymos and Vallet [33] and Gerolymos *et al.* [34] introduced a unit-vector $\mathbf{e}_I$ pointing in the direction of inhomogeneity of the turbulent field to replace the geometric wall-normals.

$$\mathbf{e}_I = e_{I_i}\mathbf{e}_i = \frac{\mathrm{grad}\left\{\dfrac{\ell_T[1 - \mathrm{e}^{-Re_T/30}]}{1 + 2\sqrt{A_2} + A^{16}}\right\}}{\left\|\mathrm{grad}\left\{\dfrac{\ell_T[1 - \mathrm{e}^{-Re_T/30}]}{1 + 2\sqrt{A_2} + A^{16}}\right\}\right\|} \tag{25}$$

The model for pressure-strain and dissipation terms, which are modelled together (cf. 2.4), reads

$$\phi_{ij} - \bar\rho\varepsilon_{ij} = \left[\phi_{ij} - \bar\rho\left(\varepsilon_{ij} - \frac{2}{3}\delta_{ij}\varepsilon\right)\right] - \frac{2}{3}\delta_{ij}\bar\rho\varepsilon$$

$$= \phi^H_{ij1} + \phi^H_{ij2} + \phi^I_{ij1} + \phi^I_{ij2} - \frac{2}{3}\delta_{ij}\bar\rho\varepsilon$$

DOI: 10.1002/fld

$$
\begin{aligned}
&= -C_1^{\mathrm{H}}\bar{\rho}\varepsilon a_{ij} - C_2^{\mathrm{H}}\left(P_{ij} - \frac{1}{3}\delta_{ij}P_{mm}\right) \\
&\quad + C_1^{\mathrm{I}}\frac{\varepsilon}{k}\left[\bar{\rho}\widetilde{u_n''u_m''}e_{\mathrm{I}_n}e_{\mathrm{I}_m}\delta_{ij} - \frac{3}{2}\bar{\rho}\widetilde{u_n''u_i''}e_{\mathrm{I}_n}e_{\mathrm{I}_j} - \frac{3}{2}\bar{\rho}\widetilde{u_n''u_j''}e_{\mathrm{I}_n}e_{\mathrm{I}_i}\right] \\
&\quad + C_2^{\mathrm{I}}\left[\phi_{nm2}^{\mathrm{H}}e_{\mathrm{I}_n}e_{\mathrm{I}_m}\delta_{ij} - \frac{3}{2}\phi_{in2}^{\mathrm{H}}e_{\mathrm{I}_n}e_{\mathrm{I}_j} - \frac{3}{2}\phi_{jn2}^{\mathrm{H}}e_{\mathrm{I}_n}e_{\mathrm{I}_i}\right] - \frac{2}{3}\delta_{ij}\bar{\rho}\varepsilon
\end{aligned} \tag{26}
$$

where the coefficients C_1^{I} and C_2^{I} contain distance from the wall effects but without using any wall-topology parameter.

$$
\begin{aligned}
C_1^{\mathrm{I}} &= 0.83\left[1 - \frac{2}{3}(C_1^{\mathrm{H}} - 1)\right]\left\|\mathrm{grad}\left\{\frac{\ell_{\mathrm{T}}[1 - \mathrm{e}^{-Re_{\mathrm{T}}/30}]}{1 + 2A_2^{0.8}}\right\}\right\| \\
C_2^{\mathrm{I}} &= \max\left[\frac{2}{3} - \frac{1}{6C_2^{\mathrm{H}}}, 0\right]\left\|\mathrm{grad}\left\{\frac{\ell_{\mathrm{T}}[1 - \mathrm{e}^{-Re_{\mathrm{T}}/30}]}{1 + 1.8A_2^{\max(0.6,A)}}\right\}\right\|
\end{aligned} \tag{27}
$$

The homogeneous terms ϕ_{ij1}^{H} and ϕ_{ij2}^{H} correspond to the forms proposed respectively by Rotta [54] and Naot *et al.* [61, 62]. The slow-part coefficient C_1^{H} proposed by Launder and Shima [37]

$$
C_1^{\mathrm{H}} = 1 + 2.58AA_2^{1/4}[1 - \mathrm{e}^{-(Re_{\mathrm{T}}/150)^2}] \tag{28}
$$

includes the anisotropic part of the dissipation term (Equation (17)). The rapid-part coefficient C_2^{H} was developed by Gerolymos and Vallet [33]

$$
\begin{aligned}
C_2^{\mathrm{H}} &= \min[1, 0.75 + 1.3\max[0, A - 0.55]] \\
&\quad \times A^{[\max(0.25, 0.5 - 1.3\max[0, A - 0.55])]}\left[1 - \max\left(0, 1 - \frac{Re_{\mathrm{T}}}{50}\right)\right]
\end{aligned} \tag{29}
$$

Despite the simple model (isotropization of production) used for the homogeneous rapid-part redistribution term ϕ_{ij2}^{H}, the particular form of the coefficient C_2^{H} (Equation (29)) in conjunction with the wall-topology-free inhomogeneous terms (Equations (26) and (27)), both improves the prediction of detached flows [34] and preserves the numerical stability close to the wall for 3-D complex flows.

The Hanjalić and Launder [46] proposal (Equation (30)), which respects the tensorial symmetry of $\widetilde{u_i''u_j''u_\ell''}$, was used to model the triple-velocity correlation

$$
-\bar{\rho}\widetilde{u_i''u_j''u_\ell''} = C_s\frac{k}{\varepsilon}\left(\bar{\rho}\widetilde{u_i''u_m''}\frac{\partial\widetilde{u_j''u_\ell''}}{\partial x_m} + \bar{\rho}\widetilde{u_j''u_m''}\frac{\partial\widetilde{u_\ell''u_i''}}{\partial x_m} + \bar{\rho}\widetilde{u_\ell''u_m''}\frac{\partial\widetilde{u_i''u_j''}}{\partial x_m}\right), \quad C_s = 0.11 \tag{30}
$$

2.6. Wall-normal-free Launder–Shima–Sharma RSM (WNF-LSS RSM)

The unit-vector $\mathbf{e}_{\mathrm{I}}$ (Equation (5)) developed by Gerolymos and Vallet [33] can be used in any Reynolds-stress model to replace the geometric unit normals to the wall which are often used in

DOI: 10.1002/fld

the redistribution or dissipation tensors closures [48, 69, 70]. In order to demonstrate the ease of implementation and the importance of using geometric-normals to the wall (or not), a wall-normal-free version of the LSS RSM was developed by Gerolymos *et al.* [34]. This model is based on the Launder–Shima–Sharma Reynolds-stress model (Section 2.4) except for the echo terms that were replaced by inhomogeneous terms (Equation (26)) while the homogeneous coefficients C_1^{H} and C_2^{H} were those of the original wall-topology-dependent Launder and Shima model [37]

$$C_1^{\mathrm{H}} = 1 + 2.58 A A_2^{1/4} [1 - \mathrm{e}^{-(Re_{\mathrm{T}}/150)^2}], \quad C_2^{\mathrm{H}} = 0.75\sqrt{A} \tag{31}$$

The functions C_1^{I} and C_2^{I} where then optimized to get the correct plane-channel-flow mean velocity and Reynolds-stress profiles [34]

$$\begin{aligned} C_1^{\mathrm{I}} &= 0.90 \left[1 - \frac{2}{3}(C_1 - 1) \right] \left\| \mathrm{grad} \left\{ \frac{\ell_{\mathrm{T}}[1 - \mathrm{e}^{-Re_{\mathrm{T}}/30}]}{1 + 1.8 A_2^{0.8}} \right\} \right\| \\ C_2^{\mathrm{I}} &= \max \left[\frac{2}{3} - \frac{1}{6C_2}, 0 \right] \left\| \mathrm{grad} \left\{ \frac{\ell_{\mathrm{T}}[1 - \mathrm{e}^{-Re_{\mathrm{T}}/30}]}{1 + 1.8 A_2^{\max(0.6, A)}} \right\} \right\| \end{aligned} \tag{32}$$

3. COMPARISON WITH EXPERIMENTS

3.1. Configurations studied

The various turbulence closures were assessed by comparison with available experimental data for the compression-ramp configurations ($M_{\mathrm{SW}} = 2.25$, $Re_{\theta_0} = 7 \times 10^3$) studied experimentally by Ardonceau [36, 71].

This test case, which includes three ramp angles ($\alpha_{\mathrm{c}} = 8$, 13, and 18°), is very interesting because experimental data include wall-static-pressure distributions, Pitot-tube-measured x-wise mean velocity ($\bar{u}$) and 3 LDV-measured Reynolds-stress components ($\overline{u'u'}$, $\overline{u'v'}$, $\overline{v'v'}$). Furthermore, the experimental supersonic wind tunnel is large enough ($z = 150\,\mathrm{mm} = 18.75\delta_0$) to assume that there is no 3-D influence. The 3-D experimental visualization of the flow using viscous coating technique on the wall [72] corroborates the 2-D nature of the interaction on the $\alpha_{\mathrm{c}} = 18°$ compression-ramp angle. The $\alpha_{\mathrm{c}} = 18°$ angle ramp includes a straight part at its end [72], which was simulated in the computations (Figure 1).

3.2. Numerical method

The flow equations are discretized on structured grids using an upwind biased ($O[\Delta x^3]$ MUSCL reconstruction) finite-volume scheme [49]. Time integration uses a local-dual-time-stepping implicit procedure with internal subiterations. Computational efficiency is achieved by a specific approximate factorization of the implicit subiterations, designed to minimize the computational cost of the turbulence-transport-equations. Convergence is still accelerated using a mean-flow-multigrid full-approximation-scheme method, where multigrid is applied on the mean-flow-variables only [50].

DOI: 10.1002/fld

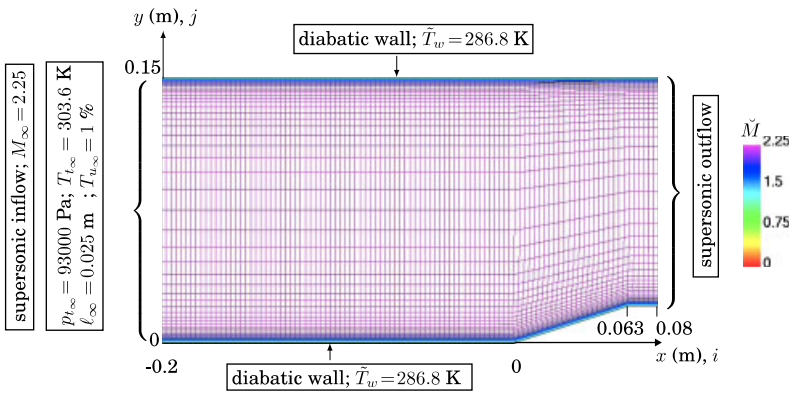

Figure 1. View of a coarse computational grid ($N_i \times N_j = 101 \times 101$, $r_j = 1.180$, $y_w^+ = 0.5$), boundary-conditions and initial flowfield Mach-number for the Ardonceau [36, 71] $\alpha_c = 18°$ compression-ramp interaction.

Table I. Computational grids used.

Grid	$N_i(N_x)$	$N_j(N_y)$	N_{j_s}	r_j	$y_w^+ \cong n_w^+$	L_x (m)	L_y (m)
Grid_C	801	801	401	1.0193	0.1	0.28	0.15
Grid_B	601	601	301	1.0270	0.1		
Grid_A	401	201	101	1.0975	0.1		

i, j: grid directions; N_i, N_j: number of points; y_w^+: non-dimensional distance of the first-grid-node away from the wall; r_j: geometric progression ratio; L_x, L_y: lengths.

3.3. *Computational grids*

In the streamwise direction (x,i) the computational grids used are uniform (Figure 1), whereas in the transverse direction (y,j) the $N_{j_s} = N_j/2 + 1$ points for each half of the computational domain (between the upper/lower wall and the centreline) were stretched geometrically with ratio r_j (Table I).

A grid-convergence study was conducted by using various grids (Table I) for the three compression-ramp angle configurations with all the four turbulence models.

Results obtained with the GV RSM and the LS k–ε model for the $\alpha_c = 18°$ configuration (Figure 2) show that grid-convergence is nearly achieved on the coarsest (401×201) grid_A (Table I). However, the GV RSM results present a slight sensitivity at the detachment point $(x = -0.02\,\text{m} = -2.5\delta_0)$ for the Reynolds stresses. Therefore, to improve accuracy in the following study, grid_C was used for the GV RSM and grid_B for all other turbulence models.

3.4. *Inflow conditions*

The inflow boundary-layer profile was adjusted to obtain a close fit to the measured integral boundary-layer parameters at the beginning of the interaction (Table II). Thus, all of the

DOI: 10.1002/fld

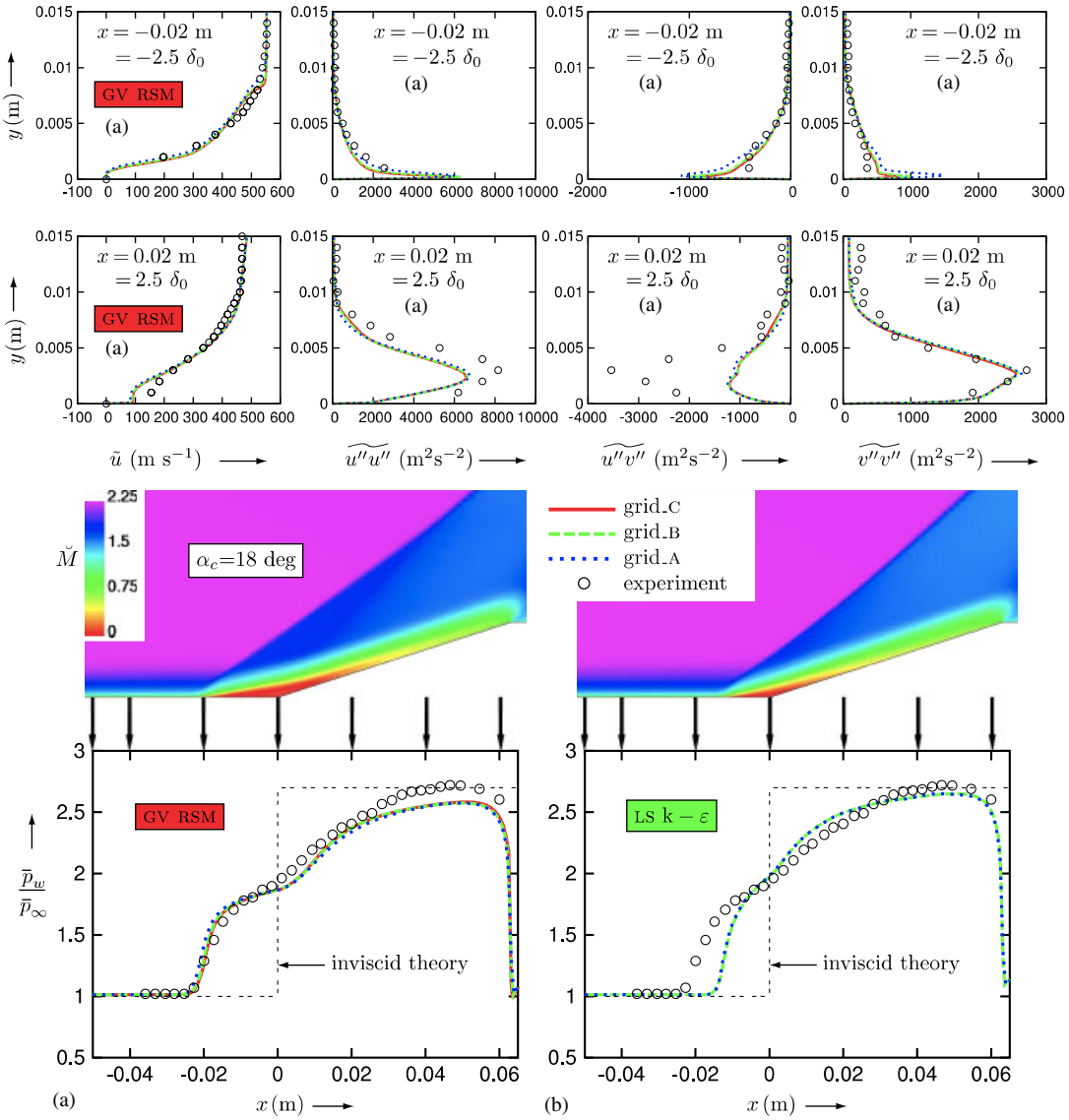

Figure 2. Grid-convergence study of longitudinal mean velocity, Reynolds stresses and wall-pressure for the $\alpha_c = 18°$ Ardonceau [36, 71] compression-ramp interaction, using the GV RSM (a), and the LS k–ε model (b), on various grids (Table I).

computations were performed using the following experimental inflow conditions:

$$T_{t_i} = 303.6\,\mathrm{K}, \quad p_{t_i} = 93\,000\,\mathrm{Pa}, \quad \tilde{T}_\mathrm{w} = T_\mathrm{r} = 286.8\,\mathrm{K} \tag{33}$$

where T_{t_i} is the inlet total temperature, p_{t_i} is the inlet total pressure, $\tilde{T}_\mathrm{w}$ is the wall temperature, and T_r is the theoretical adiabatic-wall-recovery temperature ($r_f = 0.89$) [38]. The inlet free-stream

DOI: 10.1002/fld

Table II. Inflow integral boundary-layer parameters at the beginning of the interaction.

Configuration	8, 13, 18°
$\delta_0 \times 10^3$ m (comp/exp)	8.02/8.0
$Re_{\delta_0} \times 10^{-4}$ (comp/exp)	8.0/7.8
$Re_{\theta_0} \times 10^{-3}$ (comp/exp)	6.23/7
Π_i (inflow)	0.1

$\delta_0 =$ boundary-layer thickness at the beginning of the interaction; $Re_{\delta_0} = V_\infty \delta_0 \breve{\nu}_\infty^{-1} =$ boundary-layer thickness Reynolds-number; $Re_{\theta_0} = V_\infty \theta_0 \breve{\nu}_\infty^{-1} =$ boundary-layer momentum-thickness Reynolds-number; $\theta_0 = \int_0^\delta \bar{\rho}\tilde{u}/\bar{\rho}\tilde{u}_\infty(1-\tilde{u}/\tilde{u}_\infty)\,\mathrm{d}y =$ boundary-layer momentum-thickness at the beginning of the interaction; $\Pi_i =$ Coles wake-parameter used to define the inflow profile applied as boundary condition [73].

turbulence intensity $T_{u_i} = \sqrt{\frac{2}{3}k_i}\,V_i^{-1}$ and the inlet free-stream turbulence-length-scale $\ell_{\mathrm{T}_i} = k_i^{2/3}\varepsilon_i^{-1}$ (not measured in the experiments) chosen correspond, respectively, to classical experimental values $T_{u_i} = 1\%$ and to the half-height of the experimental channel $\ell_{\mathrm{T}_i} = 25$ mm.

3.5. Wall-static-pressure distributions

Comparison of grid-converged (Table I) wall-static-pressure distribution computed using the four turbulence models, with experimental measurements, indicates that only the GV [33] wall-normal-free RSM predicts the upstream interaction length correctly for all of the three compression-ramp angles (Figure 3).

The $\alpha_c = 8°$ compression-ramp angle is not large enough to induce separation, and all of the turbulence models are in good agreement with experimental data (Figure 3). Although the LSS RSM, which contains geometric parameters, predicts the correct upstream-interaction length for the $\alpha_c = 13°$ compression-ramp angle (Figure 3), the WNF-LSS RSM (which corresponds to its wall-normal-free version) gives a better shape but with an underestimated level. Nevertheless, for the large recirculation zone observed for the $\alpha_c = 18°$ ramp angle (Figure 3), both the LSS and the WNF-LSS RSMs underestimate the upstream-interaction length. On the other hand, the GV RSM, which includes a particular form of the rapid-part redistribution coefficient C_2^{H} (Equation (29)), gives satisfactory results. The LS k–ε model fails to correctly predict detached flow and gives the worst prediction for all of the three compression-ramp angles (Figure 3). All of the four turbulence models fail to reproduce experimental data in the relaxation region after reattachment ($x \cong 0.03\,\mathrm{m} = 3.75\delta_0$). Nevertheless, we can observe a discontinuity in the experimental-data distributions at the same location. Experimental wall pressure are larger than the inviscid-theory value at the end of the compression ramp. This suggests the presence, in the experimental set-up, of a weak-shock-wave (or compression wave), coming from the upper wall, which impacts the lower-wall boundary-layer at $x \cong 0.03$ m. Therefore, discrepancies at this location are not significant in assessing the performance of the turbulence models.

DOI: 10.1002/fld

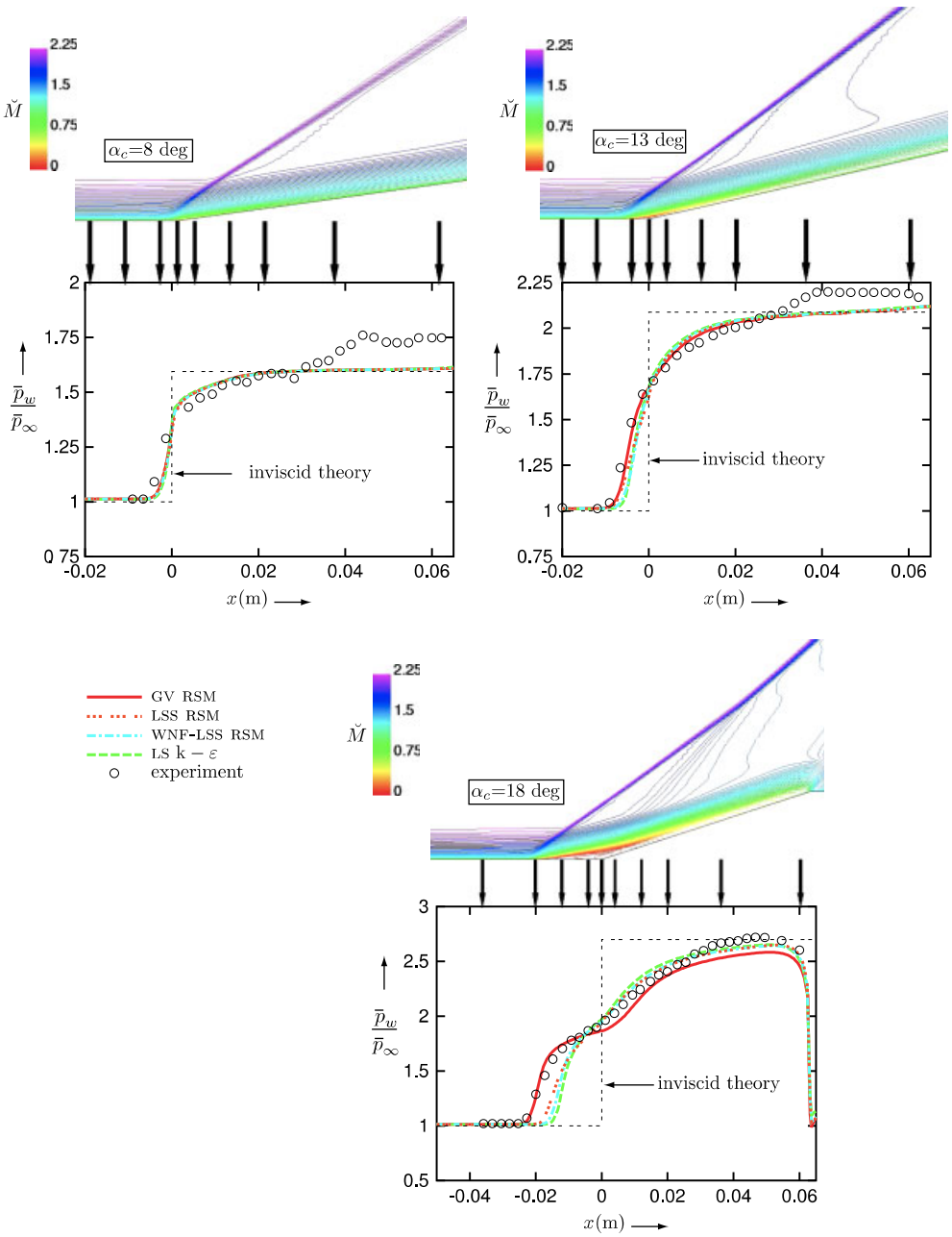

Figure 3. Comparison of grid-converged computations (Table I) with measurements [36, 71] of wall-static pressure distributions, for the Ardonceau [36, 71] $\alpha_c = 8, 13$ and 18° compression-ramp interaction ($M_\infty = 2.25$, $Re_{\theta_0} = 7 \times 10^3$) using the GV [33] and WNF-LSS [34] wall-normal-free RSMs, the LSS [37, 51] RSM with geometric normals and the LS [18] k–ε model (Mach-contours computed with the GV RSM).

DOI: 10.1002/fld

3.6. *Mean-velocity longitudinal distribution*

In all the models used, direct compressibility effects were neglected

$$|\rho'| \ll \bar{\rho}, \quad \overline{u_i''} \cong 0 \tag{34}$$

so that, Reynolds and Favre averages are assumed to be approximately equal

$$\tilde{u}_i \cong \bar{u}_i, \quad \widetilde{u_i'' u_j''} \cong \overline{u_i' u_j'} \tag{35}$$

and comparison between Pitot-tube [71] longitudinal mean velocity ($\bar{u}$) and grid-converged computed longitudinal mean velocity ($\tilde{u}$) was carried out for the three ramp angles (Figures 4–6).

Concerning the $\alpha_c = 8°$ compression-ramp angle, where the flow remains attached, all of the four turbulence models are in perfect agreement with experiments (Figure 4). A slight difference between the GV RSM and the three other turbulence models is observed (Figure 5) for the $\alpha_c = 13°$ compression-ramp angle at the detachment point ($x = -0.5\delta_0$) and near the wall at the end of the compression ramp ($x \geqslant 4.5\delta_0$).

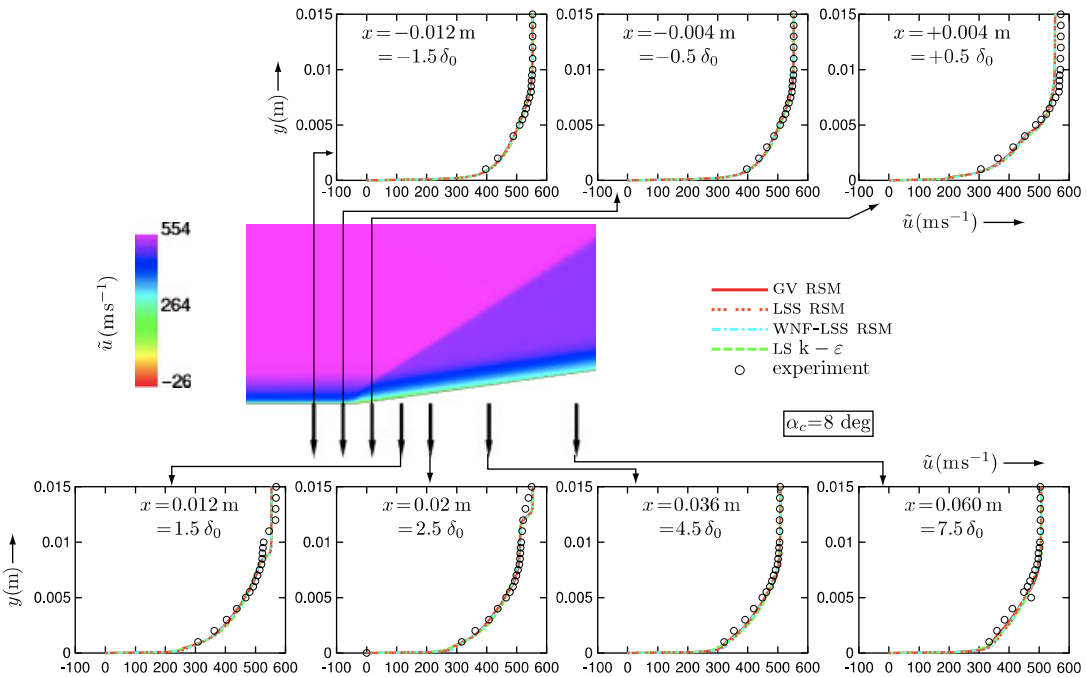

Figure 4. Comparison of grid-converged computations (Table I) with measurements [36, 71] of x-wise mean velocity ($\tilde{u}$, $\bar{u}$) at various axial stations, for the Ardonceau [36, 71] $\alpha_c = 8°$ compression-ramp interaction ($M_\infty = 2.25$, $Re_{\theta_0} = 7 \times 10^3$) using the GV [33] and WNF-LSS [34] wall-normal-free RSMs, the LSS [37, 51] RSM with geometric normals and the LS [18] k–ε model (iso x-wise mean velocity computed with the GV RSM).

DOI: 10.1002/fld

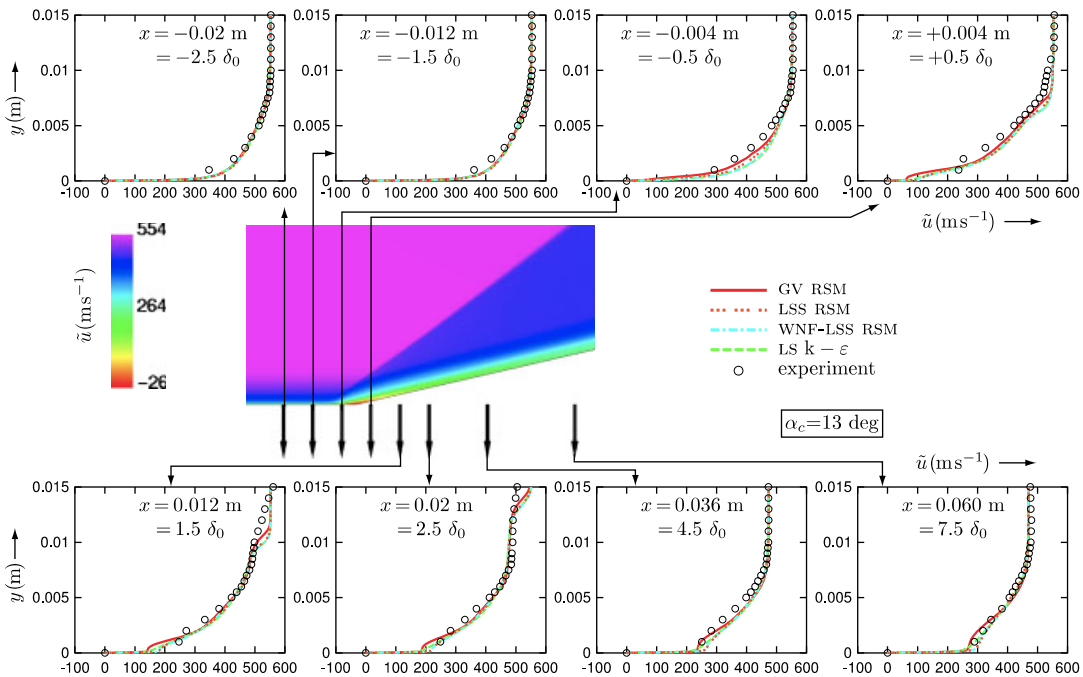

Figure 5. Comparison of grid-converged computations (Table I) with measurements [36, 71] of x-wise mean velocity ($\tilde{u}$, $\bar{u}$) at various axial stations, for the Ardonceau [36, 71] $\alpha_c = 13°$ compression-ramp interaction ($M_\infty = 2.25$, $Re_{\theta_0} = 7 \times 10^3$) using the GV [33] and WNF-LSS [34] wall-normal-free RSMs, the LSS [37, 51] RSM with geometric normals and the LS [18] k–ε model (iso x-wise mean velocity computed with the GV RSM).

As observed in the wall-pressure comparisons (Figure 3), the GV RSM performs better than the other models for the $\alpha_c = 18°$ compression-ramp interaction (Figure 6). The GV RSM predicts correctly the longitudinal mean velocity $\tilde{u}$ with the exception of the positions after the corner ($x > 0$) especially in the relaxation region ($x \geqslant 2.5\delta_0$). However, there is a discrepancy between computations and experiments (Figure 6) only for the first experimental point away from the wall, located at $y = 1\,\text{mm} = 0.125\delta_0$, which was obtained using Pitot-tube (LDV data were not used due to author remarks [71]). Dolling [7] noted, as well, that the multiscale k–ω model of Wilcox [1] underpredicts the mean-velocity profiles near the wall ($y/\delta_0 < 0.4$) in the recovery region for the 24-deg compression ramp of Settles *et al.* [20]. Actually, this is the case for all of the advanced models, such as Reynolds-stress models [4, 33], which are able to predict correctly the wall-pressure distribution for several compression-ramp angles including those with a large separation zone [5, 7, 34]. Because of the shock-wave oscillation, Dolling [7] has shown the difficulty to determine time-averaged velocity profiles from Pitot-tube measurements in this region. Consequently, the discrepancy between Pitot-measured and computed mean velocity distribution downstream the corner near the wall, must be considered with caution when assessing the turbulence model used.

The LS k–ε model seems to give the best results in the reattachment region, but this is simply because this model is not able to predict the separation zone (Figure 6).

DOI: 10.1002/fld

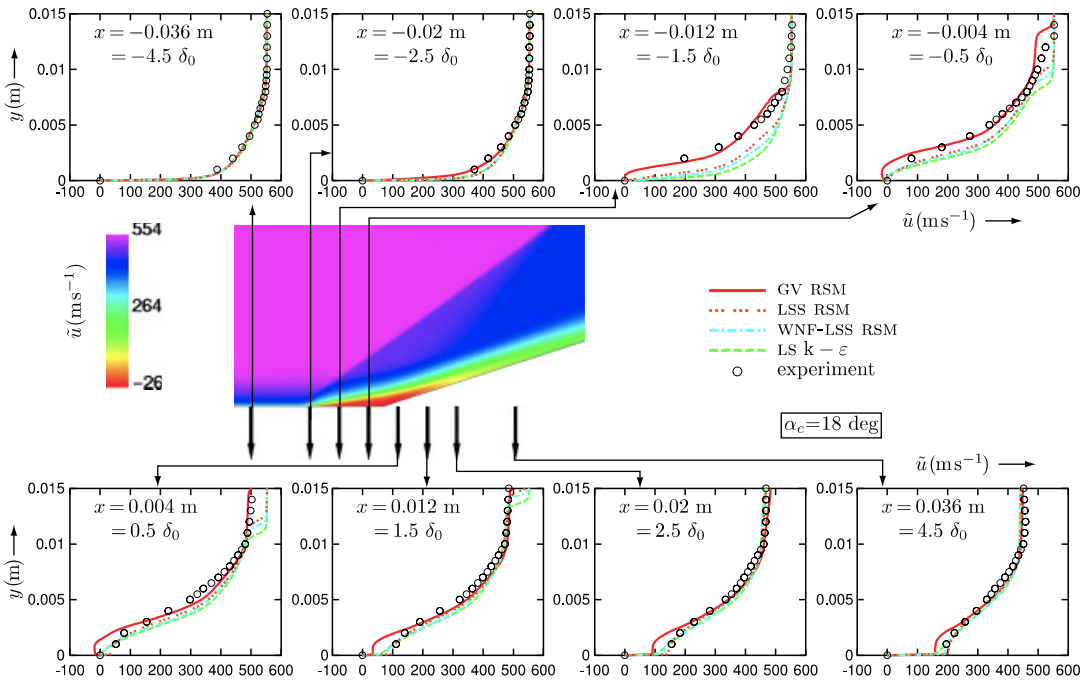

Figure 6. Comparison of grid-converged computations (Table I) with measurements [36, 71] of x-wise mean velocity ($\tilde{u}$, $\bar{u}$) at various axial stations, for the Ardonceau [36, 71] $\alpha_c = 18°$ compression-ramp interaction ($M_\infty = 2.25$, $Re_{\theta_0} = 7 \times 10^3$) using the GV [33] and WNF-LSS [34] wall-normal-free RSMs, the LSS [37, 51] RSM with geometric normals and the LS [18] k–ε model (iso x-wise mean velocity computed with the GV RSM).

3.7. *Reynolds-stresses distributions*

Comparison of measured ($\overline{u'u'}$, $\overline{u'v'}$, $\overline{v'v'}$) Reynolds-stresses with the computed ones ($\widetilde{u''u''}$, $\widetilde{u''v''}$, $\widetilde{v''v''}$) clearly shows the superiority of the RSM models over the LS k–ε model [18] (Figures 7–11), especially as far as the shear stress is concerned (Figure 11) for the $\alpha_c = 18°$ compression-ramp interaction.

3.7.1. 8 Degrees compression-ramp interaction. The three Reynolds-stress models give similar results for the two normal Reynolds-stresses components $\widetilde{u''u''}$ and $\widetilde{v''v''}$ (Figure 7). The level of the x-wise normal Reynolds-stress computed using RSMs is underestimated at the outer part of the boundary layer ($x = 0.5\delta_0$, $x = 1.5\delta_0$) and at the end of the compression ramp ($x \geqslant 4.5\delta_0$).

The y-wise component $\widetilde{v''v''}$ (note that $\widetilde{v''v''}$ is along the cartesian y-axis, and not along the normal to the surface after the beginning of the ramp at $x = 0$) is in good agreement with experimental data contrary to the LS k–ε model which overestimates the level of $\widetilde{v''v''}$ by a factor of about two. Note that the LS k–ε, which cannot take into account the redistribution between Reynolds-stresses since $\phi_{ii} = 0$, predicts almost the same level at each location both for the x-wise and the y-wise

DOI: 10.1002/fld

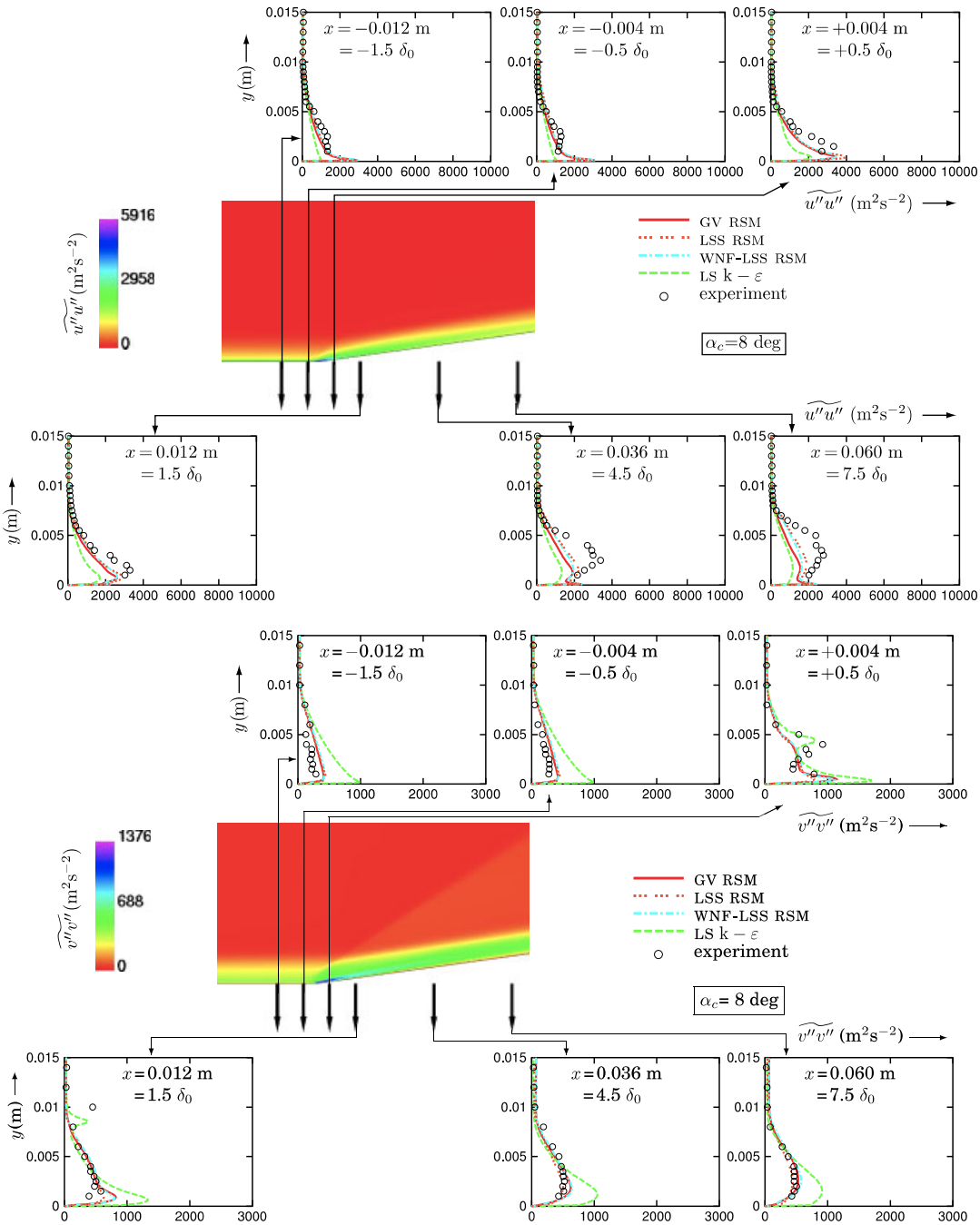

Figure 7. Comparison of grid-converged computations with measurements of normal Reynolds-stresses ($\widetilde{u''u''}$, $\widetilde{v''v''}$) at various axial stations, for the $\alpha_c = 8°$ compression-ramp angle using four turbulence models (iso x-wise and y-wise normal Reynolds-stresses computed with the GV RSM).

DOI: 10.1002/fld

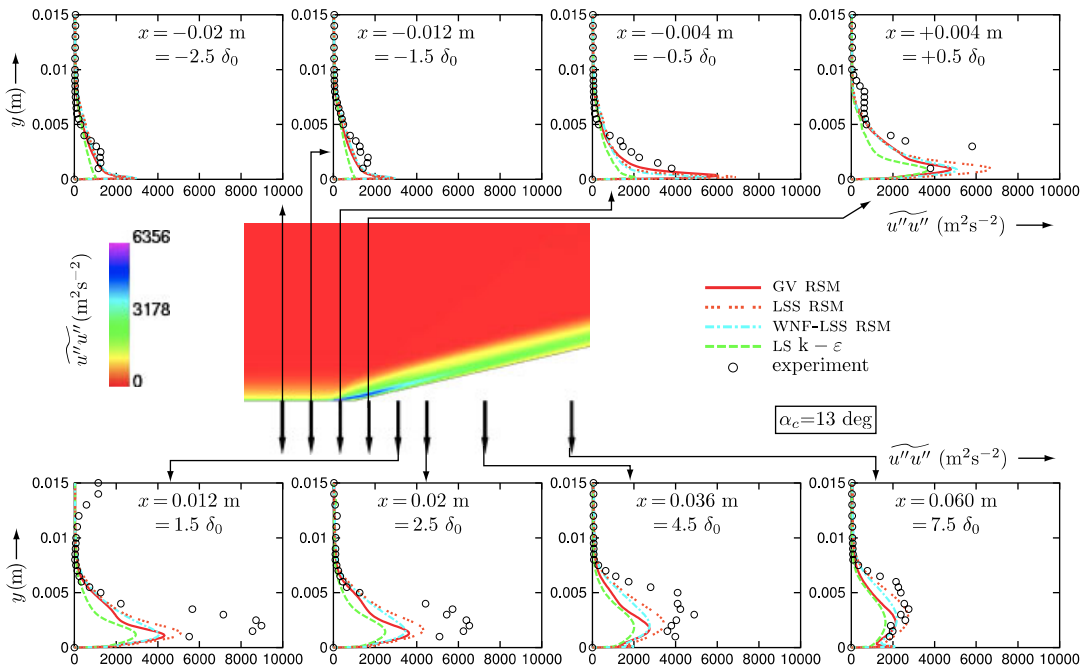

Figure 8. Comparison of grid-converged computations (Table I) with measurements [36, 71] of x-wise normal Reynolds-stress ($\widetilde{u''u''}$, $\overline{u'u'}$) at various axial stations, for the Ardonceau [36, 71] $\alpha_c = 13°$ compression-ramp interaction ($M_\infty = 2.25$, $Re_{\theta_0} = 7 \times 10^3$) using the GV [33] and WNF-LSS [34] wall-normal-free RSMs, the LSS [37, 51] RSM with geometric normals and the LS [18] k–ε model (iso x-wise normal Reynolds-stress computed with the GV RSM).

Reynolds-stresses components (for example, at $x = 7.5\delta_0$, $\widetilde{u''u''} \simeq \widetilde{v''v''} \simeq 1000\,\mathrm{m^2\,s^{-2}}$) and fails to predict turbulence quantities (Figure 7).

Surprisingly, the LS [18] k–ε model captures the high level of the y-wise component $\widetilde{v''v''}$ (Figure 7) at the outer part of the boundary layer in the shock-wave-foot region ($x = 0.5\delta_0$ and $x = 1.5\delta_0$). Actually, this good prediction seems to be a coincidence since it concerns only the $\widetilde{v''v''}$ component (not the $\widetilde{u''u''}$ component) for the $\alpha_c = 8°$ and the $\alpha_c = 13°$ compression-ramp angles (Figures 7 and 9) whereas the prediction for $\alpha_c = 18°$ case is not correct (Figure 10) at $x = 0.5\delta_0$. Furthermore, the experimental high turbulence level in this region is certainly due to the shock-wave oscillation which cannot be predicted by a steady computation using a classical statistical turbulence closure.

3.7.2. 13 Degrees compression-ramp interaction. The $\alpha_c = 13°$ compression-ramp interaction is on the verge of separating and quite different predictions of the turbulence quantities are obtained using the four turbulence models. The LS k–ε gives the worst results with a near isotropic turbulence (Figures 8 and 9). Although the three Reynolds-stress models are in better agreement with experiments, the level of the x-wise component (Figure 8) is underestimated while the y-wise component level is overestimated after the corner of the compression ramp (Figure 9). The LSS

DOI: 10.1002/fld

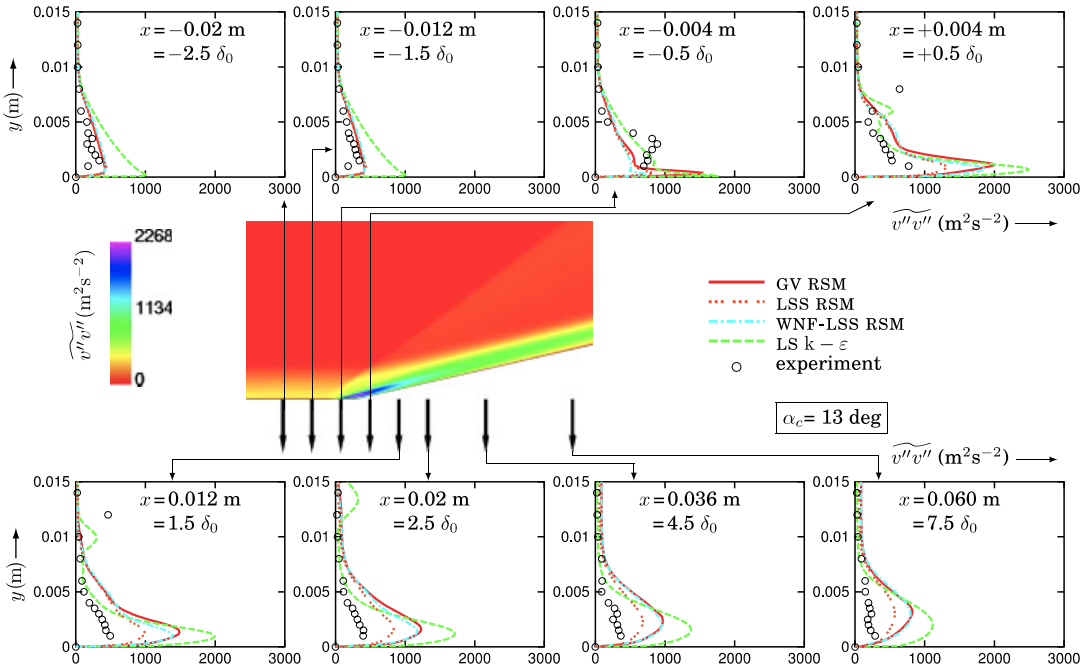

Figure 9. Comparison of grid-converged computations (Table I) with measurements [36, 71] of y-wise normal Reynolds-stress ($\widetilde{v''v''}$, $\overline{v'v'}$) at various axial stations, for the Ardonceau [36, 71] $\alpha_c = 13°$ compression-ramp interaction ($M_\infty = 2.25$, $Re_{\theta_0} = 7 \times 10^3$) using the GV [33] and WNF-LSS [34] wall-normal-free RSMs, the LSS [37, 51] RSM with geometric normals and the LS [18] k–ε model (iso y-wise normal Reynolds-stress computed with the GV RSM).

RSM, which contains the geometric normal to the wall and the distance to the wall, gives the best overall results, but the α_c angle is not high enough to bring forward the wall-normal-free effect.

3.7.3. 18 Degrees compression-ramp interaction. The $\alpha_c = 18°$ compression-ramp angle is the most interesting because the boundary-layer/shock-wave interaction produces a small separation zone at the corner, and experimental shear-stress distributions are available (Figures 10 and 11), contrary to the two other angles for which only normal stresses were measured.

For the x-wise velocity fluctuations $\widetilde{u''u''}$ (Figure 10), the GV RSM captures correctly the level and the form at the outer part of the boundary layer, mainly because of the better prediction of the velocity profile (Figure 6). Nevertheless, the GV RSM underestimates the peak of $\widetilde{u''u''}$ especially at the beginning of the interaction ($x = -1.5\delta_0$, $-0.5\delta_0$) contrary to the LSS RSM which gives the correct level at each location. However, considering that the LSS RSM predicts the detachment point ($x = -1.5\delta_0$) downstream of the experimental position ($x = -2.5\delta_0$), this relatively good $\widetilde{u''u''}$-level prediction should be regarded critically. The k–ε model fails to correctly predict the high turbulence levels at the outer edge of the boundary layer everywhere ($x \geqslant -1.5\delta_0$) and gives a level of the peaks similar of those obtained by using the LSS RSM after the corner ($x \geqslant 0.5\delta_0$).

DOI: 10.1002/fld

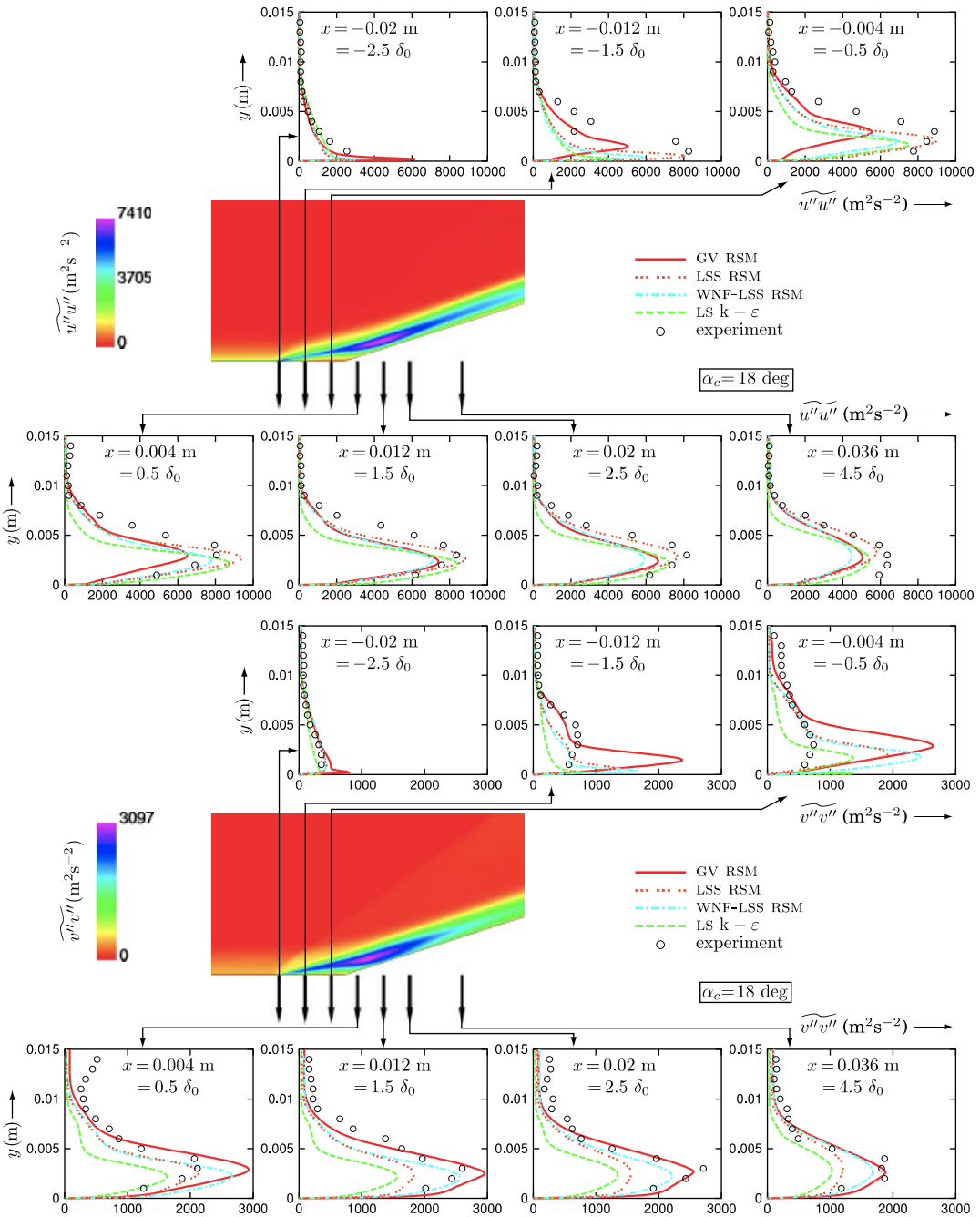

Figure 10. Comparison of grid-converged computations with measurements of normal Reynolds-stresses ($\widetilde{u''u''}$, $\widetilde{v''v''}$) at various axial stations, for the $\alpha_c = 18°$ compression-ramp angle using four turbulence models (iso x-wise and y-wise normal Reynolds-stresses computed with the GV RSM).

DOI: 10.1002/fld

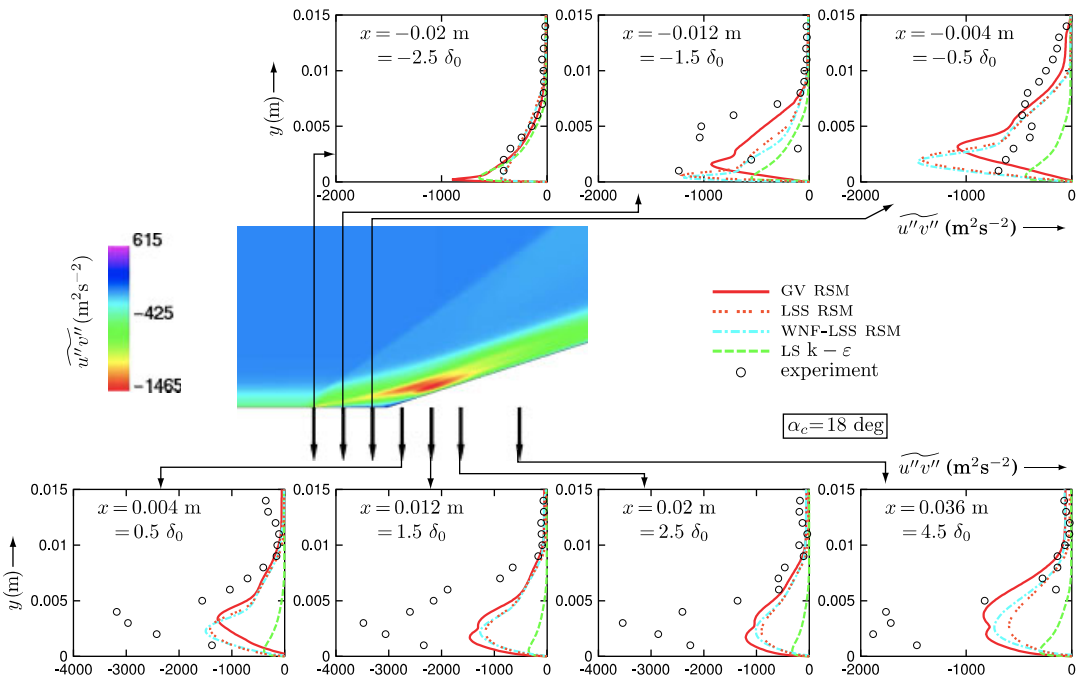

Figure 11. Comparison of grid-converged computations (Table I) with measurements [36, 71] of shear Reynolds-stress ($\widetilde{u''v''}$, $\overline{u'v'}$) at various axial stations, for the Ardonceau [36, 71] $\alpha_c = 18°$ compression-ramp interaction ($M_\infty = 2.25$, $Re_{\theta_0} = 7 \times 10^3$) using the GV [33] and WNF-LSS [34] wall-normal-free RSMs, the LSS [37, 51] RSM with geometric normals and the LS [18] k–ε model (iso shear Reynolds-stress computed with the GV RSM).

Comparison of grid-converged computed $\widetilde{v''v''}$ and measured $\overline{v'v'}$ normal stresses (Figure 10) yields some very interesting conclusions. The GV RSM (and the WNF-LSS RSM) overestimates $\widetilde{v''v''}$ at the beginning of the boundary-layer/shock-wave interaction, by about the same level that it underestimates $\widetilde{u''u''}$ (Figure 10).

However, the LSS RSM which predicts the correct level of the x-wise component (Figure 10), overestimates the level of the y-wise component (Figure 10) at the beginning of the interaction ($x \leqslant -0.5\delta_0$) and underestimates the $\widetilde{v''v''}$ level at the end of the interaction ($x \geqslant 1.5\delta_0$). This indicates that the overall energy level is not badly predicted by the two wall-normal-free RSMs contrary to the wall-topology-dependent LSS RSM, but also that it is not quite correctly redistributed along components (Ardonceau [36] has pointed out that the measurements clearly indicate that turbulence is produced on $\widetilde{u''u''}$ and then redistributed over the other components). The overall comparison of Reynolds-stresses substantiates the opinion that even better results can be obtained using the wall-normal-free models presented [34], by improving the rapid pressure-strain model used [33], eventually including the effects of compressibility following the ideas of Pantano and Sarkar [43]. On the other hand, in the relaxation region ($x \geqslant 1.5\delta_0$), the GV RSM is in very good agreement with the experimental data, whereas the LS k–ε gives the worst prediction whatever the location. Comparison of grid-converged (Table I) computed $\widetilde{u''v''}$ and measured $\overline{u'v'}$ shear-stress

DOI: 10.1002/fld

(Figure 11) indicates that the GV wall-normal-free RSM performs better than the other models because, although it fails to predict the measured levels of turbulence, it is the only one to capture the experimentally observed double-peak feature at the end of the interaction ($x \geqslant 1.5\delta_0$). The fact that the LSS and the WNF-LSS RSMs give similar results, underlines the link between the rapid-part redistribution modelling (Equation (29)) and the good prediction of the $\widetilde{u''v''}$ component particular form. The k–ε model is again very far from the experimental results with a very low level, especially in the outer part of the boundary layer. This observation indicates how the Boussinesq hypothesis (Equation (14)) completely breaks down in this part of the flow, while Reynolds-stress models, based on transport equations, are more representative of the flow physics.

3.7.4. Transport-equations budgets analysis. Analysis of the transport-equations budgets for the four Reynolds-stress-tensor components (Figures 12–15) and for the turbulent-kinetic energy (Figure 16), completes the turbulent closures evaluation.

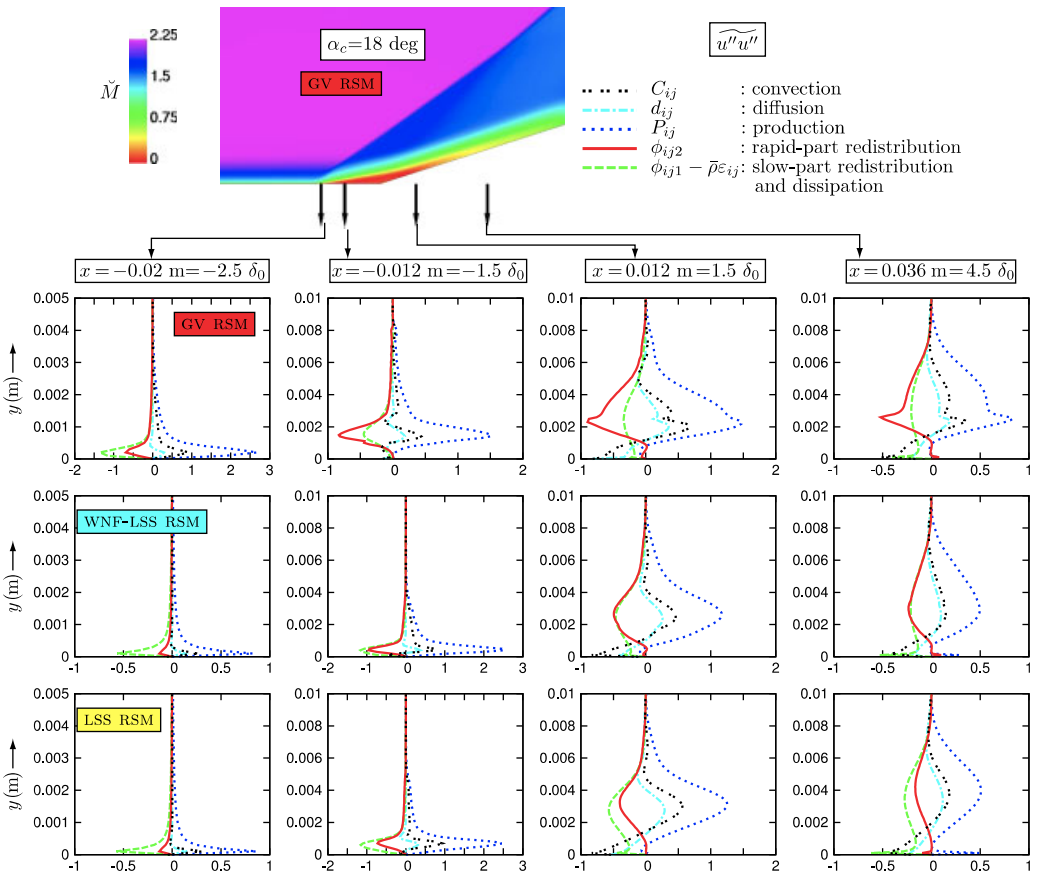

Figure 12. $\widetilde{u''u''}$ Reynolds-stress transport-equation budgets ($\times 10^{-8}$ kg m^{-1} s^{-3}) at four axial stations, for the Ardonceau [36, 71] $\alpha_c = 18°$ compression-ramp interaction ($M_\infty = 2.25$, $Re_{\theta_0} = 7 \times 10^3$) using the GV [33] and WNF-LSS [34] wall-normal-free RSMs and the LSS [37, 51] RSM with geometric normals (iso Mach number computed with the GV RSM).

DOI: 10.1002/fld

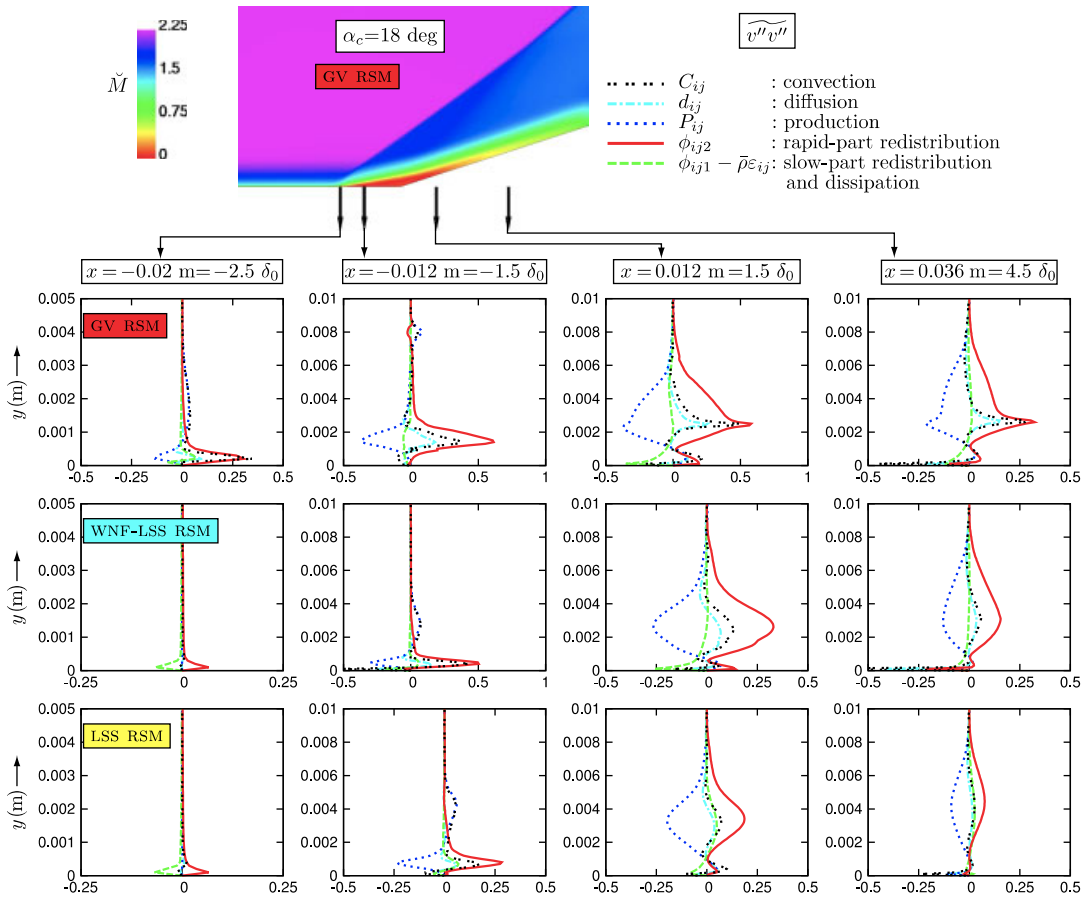

Figure 13. $\widetilde{v''v''}$ Reynolds-stress transport-equation budgets ($\times 10^{-8}$ kg m^{-1} s^{-3}) at four axial stations, for the Ardonceau [36, 71] $\alpha_c = 18°$ compression-ramp interaction ($M_\infty = 2.25$, $Re_{\theta_0} = 7 \times 10^3$) using the GV [33] and WNF-LSS [34] wall-normal-free RSMs and the LSS [37, 51] RSM with geometric normals (iso Mach number computed with the GV RSM).

Comparison of the three Reynolds-stress models for the $\widetilde{u''u''}$ component transport-equation budgets shows that the production is the most important term, especially at the detachment point ($x = -0.02\,\text{m} = -2.5\delta_0$). We can note that the GV RSM, which predicts the experimental upstream interaction length correctly, gives a higher production than the two other RSMs which predict a detachment point located at $x = -0.012\,\text{m} = -1.5\delta_0$. Since the production term is exact for full Reynolds-stress closures, the correct prediction given by the GV RSM can only be caused by the redistribution term, in particular the rapid part. Besides, the GV RSM, which uses an optimized redistribution closure (Equation (29)) gives a very important level of the rapid redistribution term compared to the LSS RSM and its wall-normal-free version WNF-LSS RSM which use the closure proposed by Launder and Shima [37] (Equation (31)). On the other hand, the level of the rapid-redistribution term is highly increased by replacing the geometric wall-normals (which are present

DOI: 10.1002/fld

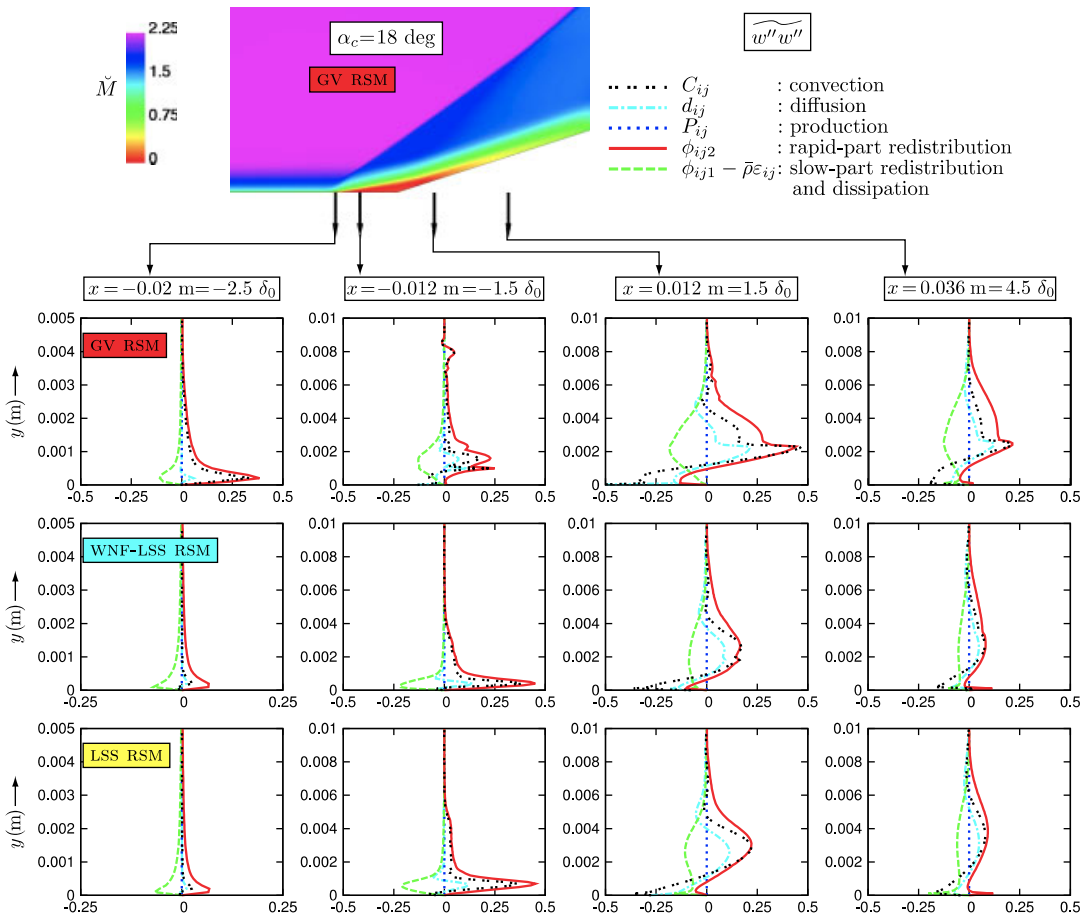

Figure 14. $\widetilde{w''w''}$ Reynolds-stress transport-equation budgets ($\times 10^{-8}$ kg m^{-1} s^{-3}) at four axial stations, for the Ardonceau [36, 71] $\alpha_c = 18°$ compression-ramp interaction ($M_\infty = 2.25$, $Re_{\theta_0} = 7 \times 10^3$) using the GV [33] and WNF-LSS [34] wall-normal-free RSMs and the LSS [37, 51] RSM with geometric normals (iso Mach number computed with the GV RSM).

in the LSS RSM) by the unit-vector $\mathbf{e}_\mathrm{I}$ (Equation (25)), which is included in the wall-normal-free version WNF-LSS RSM.

Furthermore, we can note the particular shape of every term (except for the slow-part redistribution and the dissipation terms) predicted by the GV RSM in the relaxation region (x=0.012 m=1.5δ_0 and $x = 0.036\,\mathrm{m} = 4.5\delta_0$). Consequently, this particular shape, which is also observed for the three other Reynolds-stress-tensor components (Figures 13–15), is due to the rapid-redistribution model developed by Gerolymos and Vallet [33] (Equation (29)). Note that experimental y-wise normal and shear Reynolds stresses distributions (Figures 10 and 11) present the same kind of shape, which is predicted correctly only by the GV RSM.

Concerning the $\widetilde{w''w''}$ component budget (Figure 14), the production term is zero in 2-D simulation. However, it is interesting to note that the most important contribution is due to the

DOI: 10.1002/fld

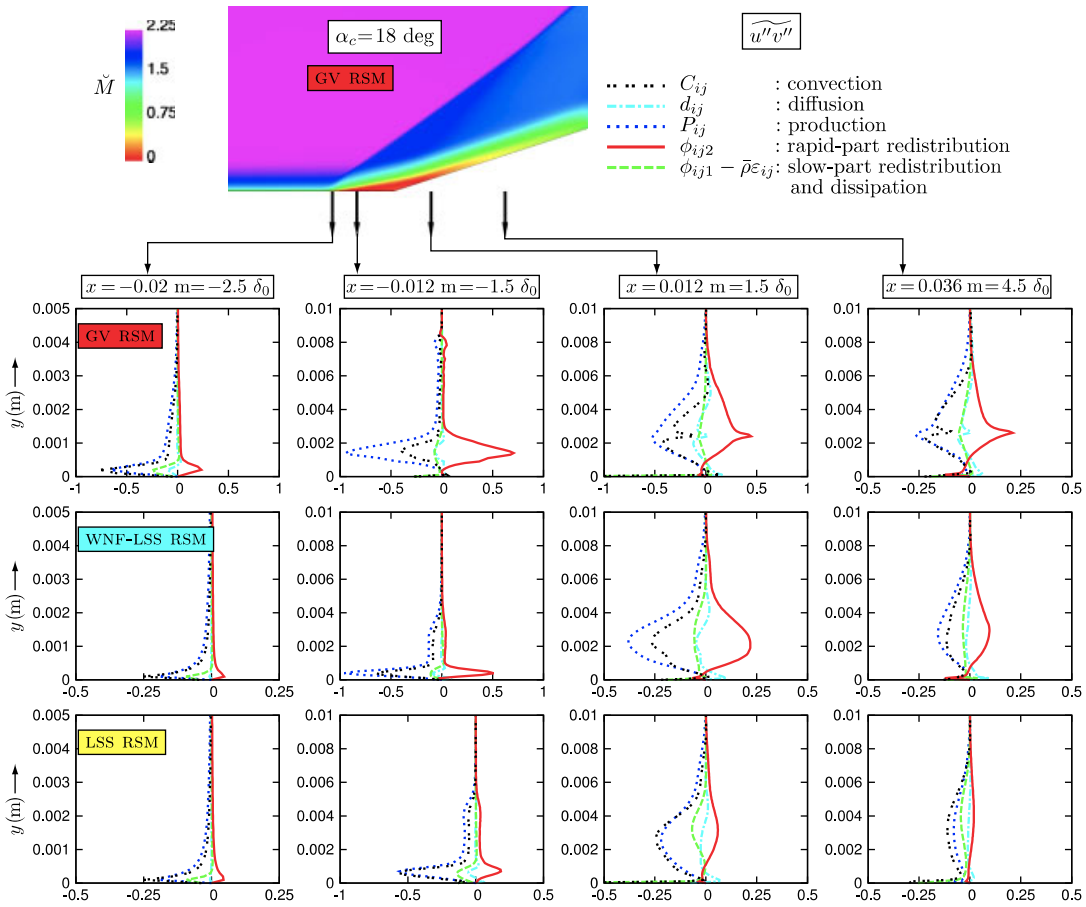

Figure 15. $\widetilde{u''v''}$ shear-stress transport-equation budgets ($\times 10^{-8}$ kg m^{-1} s^{-3}) at four axial stations, for the Ardonceau [36, 71] $\alpha_c = 18°$ compression-ramp interaction ($M_\infty = 2.25$, $Re_{\theta_0} = 7 \times 10^3$) using the GV [33] and WNF-LSS [34] wall-normal-free RSMs and the LSS [37, 51] RSM with geometric normals (iso Mach-number computed with the GV RSM).

redistribution term (rapid and slow parts) for all of the second-moment closures, especially for the GV RSM.

Finally, the LSS RSM predicts a convection contribution higher than production for the shear-stress transport-equation everywhere, contrary to its wall-normal-free version WNF-LSS RSM and the GV RSM (Figure 15). The GV RSM, which gives the best results in the relaxation region ($x \geqslant 1.5\delta_0$) for the shear-stress distribution (Figure 11), predicts a production term with a level higher by a factor two.

A comparison between the second-moment closure GV RSM and the LS k–ε model is achieved through the turbulent-kinetic-energy production P_k and the dissipation term contribution (Figure 16). The turbulent-kinetic-energy production is an exact term in the GV RSM whereas the Boussinesq hypothesis is used in the LS k–ε model. Both turbulent closures use the same

DOI: 10.1002/fld

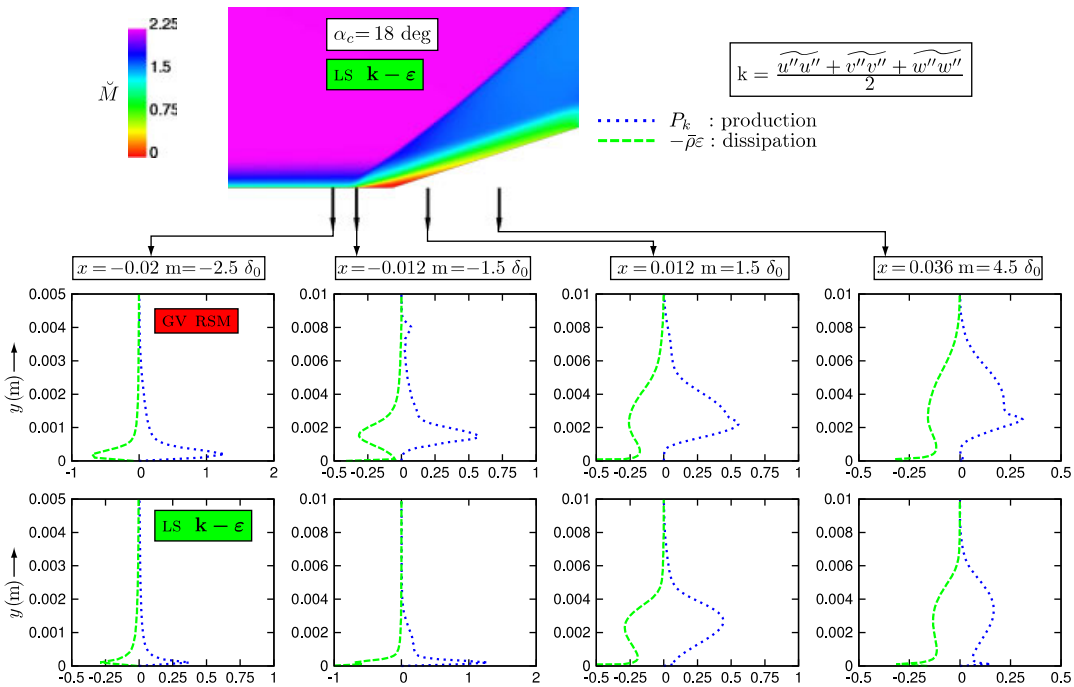

Figure 16. Turbulent-kinetic-energy production and dissipation budgets ($\times 10^{-8}$ kg m^{-1} s^{-3}) at four axial stations, for the Ardonceau [36, 71] $\alpha_c = 18°$ compression-ramp interaction ($M_\infty = 2.25$, $Re_{\theta_0} = 7 \times 10^3$) using the GV RSM [33] and the LS [18] k–ε model (iso Mach-number computed with the LS k–ε model).

dissipation equation (Equation (12)) except for the turbulent diffusion (Equation (15)), and there is no major difference in ε between the GV RSM and the LS k–ε model. On the other hand, the shape of the turbulent-kinetic-energy production is quite different. Indeed, the turbulent-kinetic-energy production predicted by the Reynolds-stress model is close to zero near the wall in the relaxation region with a pronounced peak away from the wall. Furthermore the level of the production is more important for the GV RSM than for the LS k–ε.

3.8. A note on experimental shock-wave unsteadiness

In the $\alpha_c = 18°$ compression-ramp comparisons, the GV RSM is in good agreement with experiment at the outer part of the boundary layer except for the $x = 0.5\delta_0$ location for both the y-wise normal and the shear Reynolds-stresses (Figures 10 and 11) where the experimental turbulence level is very high. This discrepancy exists also for the $\alpha_c = 13°$ compression-ramp angle at $x = -0.5\delta_0$ and $x = 0.5\delta_0$ for both the $\widetilde{u''u''}$ and the $\widetilde{v''v''}$ components (Figures 8 and 9). Small experimental oscillations of the shock-wave offer an explanation which is able to justify for all of the three compression-ramp angles (1) the high experimental turbulence level at the outer part of the boundary layer in the separation zone, (2) the bad level of the computed Reynolds-stresses with an overall satisfactory energy level, and (3) the good prediction of the wall-pressure and of the mean-velocity profiles. Indeed, numerous experimental studies, which are described in detail

DOI: 10.1002/fld

by Dolling [35] and Knight *et al.* [12], have measured the unsteadiness of the shock-wave, especially in separated supersonic flows. However, most of the experimental data [20, 36] used to assess turbulence closures are time averaged and because of the low frequency of the shock-wave oscillation (difficulty to reach statistical convergence and possibility to have a combined set-up oscillation), appropriate caution should be used when these measurements are compared with computational results. Furthermore, statistic turbulence closures (RANS models) are not able to predict unsteady flows, except for deterministic cases associated with time-dependent boundary-conditions such as fluctuating back- or inlet-pressure, or moving/deforming solid boundaries. Consequently, only unsteady computations, which are able to take into account the experimental shock-wave oscillation such as large eddy simulation (LES) or hybrid very large eddy simulation using multi-equation statistical models for the unresolved stresses (RSM-VLES), should be used to improve the Reynolds-stresses distributions in compression-ramp configurations. Notice, nonetheless that if the low-frequency shock-wave oscillations are associated with large scale wind tunnel circuit phenomena, additional modelling of set-up oscillation might be necessary.

4. CONCLUSIONS

In the present work, we studied the performance of second-moment closures for compression-ramp oblique-shock-wave/turbulent-boundary-layer interaction, focusing on the prediction of turbulent correlations, and on the budgets of the associated transport equations. To this purpose, we chose an experimental database [36, 71] with detailed measurements of the Reynolds-stresses, and which has also the advantage of relatively compressibility effects because of the relatively low Mach number $M_{sw} = 2.25$. Three low-Reynolds number Reynolds-stress models and a standard linear k–ε model were assessed in three supersonic compression-corner flows studied experimentally by Ardonceau [36, 71]. The present work examined (1) the effect of eliminating the geometric parameters in the Launder and Shima [37] RSM (with the ε transport equation of the Launder and Sharma [18] k–ε closure), (2) the importance of the redistribution term in detached flows, and (3) the possible impact of the experimental shock-wave oscillation on statistical-closures (RANS models) predictions. The RSM developed by Gerolymos and Vallet [33], which is wall-topology free and includes an optimized rapid-redistribution closure, predicts correctly the wall-pressure and the mean-velocity distributions for all of the three compression-ramp angles. On the other hand, the Launder and Shima [37] RSM, which includes the distance from the wall and the normal to the wall, seems unsuitable for the larger angle ($\alpha_c = 18°$). Furthermore, the LSS RSM and its wall-topology-free version (WNF-LSS RSM) underestimate the upstream-interaction length for the $\alpha_c = 13°$ and the $\alpha_c = 18°$ compression-ramp angles. Besides, a detailed analysis of transport-equation budgets for several Reynolds-stresses and for the turbulent-kinetic energy shows that the rapid-part redistribution model proposed by Gerolymos and Vallet [33] increases the Reynolds-stresses production and improves the shape of the Reynolds-stresses profiles. Consequently, the redistribution-term modelling is of prime importance in supersonic compression-corner flows especially when an important separation zone occurs. The Launder and Sharma [18] k–ε closure, which does not contain a redistribution term, completely fails to reproduce the anisotropic turbulence structure for all of the three compression-ramp angles.

Reynolds-stress models offer high predictive potential compared with lower-order statistical turbulence closures such as standard linear k–ε models. An appropriate wall-topology-free redistribution-term model is able to predict the mean-flow distributions of shock-wave/boundary-layer interaction both for detached or unseparated flows. Nevertheless, a discrepancy is observed

DOI: 10.1002/fld

for the Reynolds-stresses profiles especially in the shock-wave foot region which could be caused by the experimental low-frequency shock-wave oscillation. Unfortunately, the main weakness of second-moment closures is their inability to simulate non-deterministic unsteadiness which is due to turbulence. Thus, to improve the Reynolds-stress prediction in this region, an hybrid RSM-VLES model that uses a Reynolds-stress closure to compute the unresolved stresses [74] should be used.

ACKNOWLEDGEMENTS

The computations presented in this work were performed at the Institut pour le Développement des Ressources en Informatique Scientifique (IDRIS), where computer resources were made available by the Comité Scientifique.

REFERENCES

1. Wilcox DC. Supersonic compression-corner applications of a multiscale model for turbulent flows. *AIAA Journal* 1990; **28**:1194–1198.
2. Knight DD, Horstman CC, Bogdonoff S. Structure of supersonic turbulent flow past a swept compression corner. *AIAA Journal* 1992; **30**:890–896.
3. Lee J, Taulbee DB, Holden MS. Study of turbulence on supersonic compression surfaces using Reynolds stress model. *AIAA Journal* 1992; **30**:1738–1746.
4. Haidinger FA, Friedrich R. Numerical simulation of strong shock/turbulent boundary layer interaction using a Reynolds stress model. *Zeitschrift für Flugwissen schaften Weltraumforsch* 1995; **19**:10–18.
5. Ribault CL, Friedrich R. Investigation of transport equations for turbulent heat fluxes in compressible flows. *International Journal of Heat and Mass Transfer* 1997; **40**:2721–2738.
6. Rizzetta DP. Evaluation of explicit algebraic Reynolds-stress models for separated supersonic flows. *AIAA Journal* 1998; **36**:24–30.
7. Dolling DS. High-speed turbulent separated flows: consistency of mathematical models and flow physics. *AIAA Journal* 1998; **36**:725–732.
8. Liou WW, Huang G, Shih TH. Turbulence model assessment for shock-wave/turbulent-boundary-layer interaction in transonic and supersonic flows. *Computers and Fluids* 2000; **29**:275–299.
9. Matesanz A, Velázquez A. EARSM finite element solver for the study of turbulent 3-D compressible separated flows. *Computer Methods in Applied Mechanics and Engineering* 2000; **190**:989–1004.
10. Rizzetta DP, Visbal MR. Application of large-Eddy simulation to supersonic compression ramps. *AIAA Journal* 2002; **40**:1574–1581.
11. Xiao X, Edwards JR, Hassan HA, Baurle RA. Inflow boundary conditions for hybrid large Eddy/Reynolds averaged Navier–Stokes simulations. *AIAA Journal* 2003; **41**:1481–1489.
12. Knight D, Yan H, Panaras AG, Zheltovodov A. Advances in CFD prediction of shock wave turbulent boundary layer interactions. *Progress in Aerospace Sciences* 2003; **39**:121–184.
13. Gerolymos GA, Sauret E, Vallet I. Oblique-shock-wave/boundary-layer interaction using near-wall Reynolds-stress models. *AIAA Journal* 2004; **42**:1089–1100.
14. von Kaenel R, Kleiser L, Adams NA, Vos JB. Large-eddy simulation of shock-turbulence interaction. *AIAA Journal* 2004; **42**:2516–2528.
15. Sinha K, Mahesh K, Candler GV. Modeling the effect of shock unsteadiness in shock/turbulent boundary-layer interactions. *AIAA Journal* 2005; **43**:586–594.
16. Chien KY. Predictions of channel and boundary-layer flows with a low-Reynolds number turbulence model. *AIAA Journal* 1982; **20**:33–38.
17. Jones WP, Launder BE. The prediction of laminarization with a 2-equation model of turbulence. *International Journal of Heat and Mass Transfer* 1972; **15**:301–314.
18. Launder BE, Sharma BI. Application of the energy dissipation model of turbulence to the calculation of flows near a spinning disk. *Letters in Heat and Mass Transfer* 1974; **1**:131–138.
19. Wilcox DC. Reassessment of the scale-determining equation for advanced turbulence models. *AIAA Journal* 1988; **26**:1299–1310.

DOI: 10.1002/fld

20. Settles GS, Bogdonoff SM, Vas IE. Incipient separation of a supersonic turbulent-boundary-layer at high-Reynolds-numbers. *AIAA Journal* 1976; **14**:50–56.
21. Jones WP, Launder BE. The calculation of low-Reynolds-number phenomena with a 2-equation model of turbulence. *International Journal of Heat and Mass Transfer* 1973; **16**:1119–1130.
22. Kuntz DW, Amatucci VA, Addy AL. Turbulent boundary-layer properties downstream of the shock-wave/boundary-layer interaction. *AIAA Journal* 1987; **25**:668–675.
23. Robinson DF, Hassan HA. Further development of the k–ζ (enstrophy) turbulence closure model. *AIAA Journal* 1998; **36**:1825–1833.
24. Zheltovodov AA, Zaulichniy EG, Trofimov VM, Yakolev VN. Heat transfer and turbulence study in compressible separated flows. *Preprint 22-87*. Institute of Theoretical and Applied Mechanics, Russian Academy of Sciences, Novosobirsk, Russia 1987.
25. Coakley TJ, Huang PG. Turbulence modeling for high speed flows. *AIAA Paper 92-0436*, 1992.
26. Gerlinger P, Brüggemann D. Multigrid convergence acceleration for turbulent supersonic flows. *International Journal for Numerical Methods in Fluids* 1997; **24**:1019–1035.
27. Menter FR. 2-Equation Eddy-viscosity turbulence models for engineering applications. *AIAA Journal* 1994; **32**:1598–1605.
28. Craft TJ, Launder B, Suga K. Development and application of a cubic Eddy-viscosity model of turbulence. *International Journal of Heat and Fluid Flow* 1996; **17**:108–115.
29. Gatski TB, Speziale CG. On explicit algebraic stress models for complex turbulent flows. *Journal of Fluid Mechanics* 1993; **254**:59–78.
30. Abid R, Morrison JH, Gatski TB, Speziale CG. Prediction of aerodynamic flows with a new explicit algebraic stress model. *AIAA Journal* 1996; **34**:2632–2635.
31. Wilcox DC. Dilatation–dissipation corrections for advanced turbulence models. *AIAA Journal* 1992; **30**:2639–2646.
32. Wilcox DC. Progress in hypersonic turbulence modelling. *AIAA Paper 91-1785*, 1991.
33. Gerolymos GA, Vallet I. Wall-normal-free near-wall Reynolds-stress closure for 3-D compressible separated flows. *AIAA Journal* 2001; **39**:1833–1842.
34. Gerolymos GA, Sauret E, Vallet I. Contribution to the single-point-closure Reynolds-stress modelling of inhomogeneous flow. *Theoretical Computational Fluid Dynamics* 2004; **17**:407–431.
35. Dolling DS. Fifty years of shock-wave/boundary-layer interaction research: what next? *AIAA Journal* 2001; **39**:1517–1531.
36. Ardonceau PL. The structure of turbulence in a supersonic shock-wave/boundary-layer interaction. *AIAA Journal* 1984; **22**:1254–1262.
37. Launder BE, Shima N. 2-Moment closure for the near-wall sublayer: development and application. *AIAA Journal* 1989; **27**:1319–1325.
38. Smits AJ, Dussauge JP. *Turbulent Shear Layers in Supersonic Flow*. AIP Press: Woodbury, NY, U.S.A., 1996, ISBN: 1-56396-260-8.
39. Vandromme D, Minh HH. About the coupling of turbulence closure models with averaged Navier–Stokes equations. *Journal of Computational Physics* 1986; **65**:386–409.
40. Gerolymos GA. Implicit multiple-grid solution of the compressible Navier–Stokes equations using k–ε turbulence closure. *AIAA Journal* 1990; **28**:1707–1717.
41. Nagano Y, Kim C. A two-equation model for heat transport in wall turbulent shear flows. *ASME Journal of Heat Transfer* 1988; **110**:583–589.
42. So RMC, Gatski TB, Sommer TP. Morkovin hypothesis and the modeling of wall-bounded compressible turbulent flows. *AIAA Journal* 1998; **36**:1583–1592.
43. Pantano C, Sarkar S. A study of compressibility effects in the high-speed turbulent shear layer using direct simulation. *Journal of Fluid Mechanics* 2002; **451**:329–371.
44. Sauret E, Vallet I. Near-wall turbulent pressure diffusion modelling and influence in 3-D secondary flows. *ASME Journal of Fluid Engineering* 2007; **129**:634–642.
45. Vallet I. Reynolds-stress modelling of 3-D secondary flows with emphasis on turbulent diffusion closure. *ASME Journal of Applied Mechanics* 2007, in press.
46. Hanjalić K, Launder BE. A Reynolds stress model of turbulence and its application to thin shear flows. *Journal of Fluid Mechanics* 1972; **52**:609–638.
47. Launder BE, Tselepidakis DP, Younis BA. A second-moment closure study of rotating channel flow. *Journal of Fluid Mechanics* 1987; **183**:63–75.
48. Jakirlić S, Hanjalić K. A new approach to modelling near-wall turbulence energy and stress dissipation. *Journal of Fluid Mechanics* 2002; **459**:139–166.

DOI: 10.1002/fld

49. Chassaing JC, Gerolymos GA, Vallet I. Efficient and robust Reynolds-stress model computation of 3-D compressible flows. *AIAA Journal* 2003; **41**:763–773.
50. Gerolymos GA, Vallet I. Mean-flow-multigrid for implicit Reynolds-stress-model computations. *AIAA Journal* 2005; **43**:1887–1898.
51. Gerolymos GA, Vallet I. Near-wall Reynolds-stress 3-D transonic flows computation. *AIAA Journal* 1997; **35**:228–236.
52. Shima N. Low-Reynolds-number second-moment closure without wall-reflection redistribution terms. *International Journal of Heat and Fluid Flow* 1998; **19**:549–555.
53. Chou PY. On velocity correlations and the solutions of the equations of turbulent fluctuations. *Quarterly of Applied Mathematics* 1945; **3**:38–54.
54. Rotta J. Statistische Theorie nichthomogener Turbulenz—1. Mitteilung. *Zeitschrift fuer Physik* 1951; **129**: 547–572.
55. Lumley JL. Second order modeling of turbulent flows. *Prediction Methods for Turbulent Flows*, VKI Lecture Series. von Kármán Institute for Fluid Dynamics: Belgium, 1979.
56. Launder BE, Li SP. On the elimination of wall-topography parameters from 2-moment closure. *Physics of Fluids* 1994; **6**:999–1006.
57. Djenidi L, Antonia RA. Modeling of the Reynolds-stress transport equation. *AIAA Journal* 1997; **35**:450–455.
58. So RMC, Yuan SP. A geometry independent near-wall Reynolds-stress closure. *International Journal of Engine Science* 1999; **37**:33–57.
59. Kim J, Moin P, Moser R. Turbulence statistics in fully developed channel flow at low-Reynolds-number. *Journal of Fluid Mechanics* 1987; **177**:133–166.
60. Gerolymos GA, Neubauer J, Sharma VC, Vallet I. Improved prediction of turbomachinery flows using near-wall Reynolds-stress model. *ASME Journal of Turbomachinery* 2002; **124**:86–99.
61. Naot D, Shavit A, Wolfshtein M. Interactions between components of the turbulent velocity correlation tensor due to pressure fluctuations. *Israel Journal of Technology* 1970; **8**:259–269.
62. Naot D, Shavit A, Wolfshtein M. 2-point-correlation model and the redistribution of Reynolds-stresses. *Physics of Fluids* 1973; **16**:738–743.
63. Launder BE, Reece GJ, Rodi W. Progress in the development of a Reynolds-stress turbulence closure. *Journal of Fluid Mechanics* 1975; **68**:537–566.
64. Shir CC. A preliminary numerical study of atmospheric turbulent flows in the idealized planetary boundary-layer. *Journal of Atmospheric Sciences* 1973; **30**:1327–1339.
65. Gibson MM, Launder BE. Ground effects on pressure fluctuations in the atmospheric boundary-layer. *Journal of Fluid Mechanics* 1978; **86**:491–511.
66. Lumley JL. Computational modeling of turbulent flows. *Advances in Applied Mechanics* 1978; **18**:123–176.
67. Daly BJ, Harlow FH. Transport equations in turbulence. *Physics of Fluids* 1970; **13**:2634–2649.
68. Craft TJ, Launder B. A Reynolds-stress model designed for complex geometries. *International Journal of Heat and Fluid Flow* 1996; **17**:245–254.
69. Lai YG, So RMC. On near-wall turbulent flow modelling. *Journal of Fluid Mechanics* 1990; **221**:641–673.
70. Hanjalić K, Jakirlić S. A model of stress dissipation in second-moment closures. *Applied Science Research* 1993; **51**:513–518.
71. Fernholz HH, Finley PJ, Dussauge JP, Smits AJ. A survey of measurements and measuring techniques in rapidly distorted compressible turbulent boundary layers. *AGARDograph 315*, AGARD, 1989.
72. Ardonceau PL. Etude de l'Interaction Onde-de-Choc/Couche-Limite supersonique. *Doctorat*, Université de Poitiers, Poitiers [F] 1981.
73. Gerolymos GA, Sauret E, Vallet I. Influence of inflow-turbulence in shock-wave/turbulent-boundary-layer interaction computations. *AIAA Journal* 2004; **42**:1101–1106.
74. Gerolymos GA, Sénéchal D, Vallet I. RSM-VLES multiblock implicit solver using high-order upwind schemes. *AIAA Paper 2006-3909*, *36*. *AIAA Fluid Dynamics Conference*, 5–8 June 2006, San Fransisco, CA, U.S.A., 2006.

DOI: 10.1002/fld